Review

Expert Opinion

Applications for site-directed molecular imaging agents coupled with drug delivery potential

Hui Wang & Xiaoyuan Chen†
Stanford University School of Medicine, The Molecular Imaging Program at Stanford (MIPS), Department of Radiology and Bio-X Program, 1201 Welch Rd, P093, Stanford, CA 94305-5484, USA

Molecular imaging allows non-invasive characterization and quantification of biological processes at cellular and molecular level. Such technologies make it possible to enhance our understanding of drug activity and pharmokinetic properties, and therefore aid decisions to select candidates that are most likely to benefit from targeted drug therapy. Targeted DDSs are nanometer-sized carrier materials designed for improving the biodistribution of systemically applied (chemo-)therapeutics by strictly localizing its pharmacological activity to the site or organ of action. The parallel development of molecular imaging and targeted drug delivery offers great challenges and opportunities for a single multifunctional platform technology, combining targeted motif, therapeutic agents and imaging agents for imaging guided drug delivery. This review article summarizes the synthesis and characterization of various biomaterials that carry targeting motifs, imaging tags and therapeutic agents as theragnostics.

Keywords: molecular imaging, molecular therapy, nanoplatform, theragnostics

Expert Opin. Drug Deliv. (2009) 6(7):745-768

1. Introduction

Molecular imaging attempts to characterize and quantify biological processes at the cellular and subcellular level in intact living objects. Such technologies therefore have great potential to enhance our understanding of disease and drug activity during drug development. The use of imaging end points instead of time-consuming dissection and histology can significantly decrease the workload involved in tissue analysis and thereby speed up the evaluation of the drug candidate. Imaging might provide information about biomarkers of a disease process and therefore help to aid decisions in patient stratification. In preclinical small animal studies, since imaging methods are non-invasive, they allow for longitudinal studies in a single animal, which increases the statistical relevance of the study. Imaging also provides important information on the optimal timing and dosing of drugs. Targeted nanometric contrast agents have been developed based on polymers, lipids and/or proteins that carry radionuclides, paramagnetic elements and/or fluorescent probes suitable for imaging.

Targeted drug delivery is defined in the broadest sense, that is, to optimize a drug's therapeutic index by strictly localizing its pharmacological activity to the site or organ of action. If successful, targeted drug delivery will reduce the drug toxicity, reduce the drug dose and increase the treatment efficacy. With the ability to realize local drug delivery, it is important to assure that the therapy is in the right region, that the drug concentration and the resulting physiological reaction are sufficient and to intervene if necessary. However, there are several challenges

informa
healthcare

10.1517/17425240902889751 © 2009 Informa UK Ltd ISSN 1742-5247

for the effective evaluation of these drugs in preclinical and clinical studies. These challenges include identifying the 'correct', biologically active concentration and dose schedule, selecting the patients likely to benefit from treatment, monitoring inhibition of the target protein or pathway, and assessing the therapy response. The parallel development of molecular imaging and targeted drug delivery may offer great potential for a single multifunctional system, containing both therapeutic and imaging components, for imaging-guided drug delivery. Such multifunctional carriers will ultimately allow for real-time imaging of drug location, drug local concentration, drug release kinetics combined with improved treatment efficacy through the use of drug delivery system (DDS). In addition, by choosing appropriate molecular imaging targeting ligands to associate with the DDS, imaging will also give information about the status of receptor expression level, and thereby may help to predict therapeutic efficacy. This system will lead to a more personalized approach in disease management, with each individual patient being closely monitored. The physicians can thus decide on the best suitable therapy based on the individual patient's status and response.

The aim of this review is to describe the development of imaging probes with potential for targeted drug delivery vehicles, the benefits that targeted DDS development may gain from incorporating an imaging component and the potential of formulating imaging and therapy within a single multifunctional carrier for disease management. The review will start by introducing imaging probes for radionuclide imaging, optical imaging, ultrasound imaging and MR imaging, then theragnostics that carry both imaging tags and therapeutics will be examined in detail. Finally, perspectives on the development of multifunctional carriers for both therapeutic and imaging purposes will be explored.

2. Molecular imaging agents coupled with drug delivery potential

The current molecular imaging techniques include radionuclide imaging, optical imaging, targeted ultrasound (US), molecular magnetic resonance imaging (mMRI) and magnetic resonance spectroscopy (MRS). Single-photon emission computed tomography (SPECT) and positron emission tomography (PET) are the most commonly used radionuclide imaging modalities, offering the potential to detect molecular and cellular changes of diseases, but they suffer from relatively poor spatial resolution with the currently available technology. Optical imaging is cost-effective and highly sensitive but with difficulty of quantification and high background signal due to tissue autofluorescence. Limited tissue penetration and scattering are two other problems optical imaging encounters. MRI/MRS and US are characterized by high spatial resolution but they are unable to detect diseases until tissue structural or functional changes are large enough to be detected. For each imaging modality, we will briefly introduce the basic principles and give examples of targeted imaging probes that are loaded with therapeutics.

2.1 Radiolabeled drug delivery system

PET and SPECT are the most commonly used radionuclide imaging modalities [1]. SPECT depends on a radionuclide that emits gamma rays with energies between roughly 71 keV (^{210}Tl) and 300 keV (^{67}Ga) and on dedicated lead collimators. SPECT involves the acquisition of images from various positions using a gamma camera rotating around the subject of interest. The most popular SPECT radionuclides are ^{67}Ga, ^{99m}Tc, ^{111}In and ^{123}I. SPECT provides excellent quantification in small animals when dedicated scanners are used. However, in clinics, quantification of SPECT data is much less accurate due to the uncertainty in attenuation correction. In addition, SPECT has limited temporal resolution, which can be partially solved by using radiolabeled agents with long biological and physical half-life [2,3]. PET is based on radionuclides that decay by emitting positrons, antiparticles to electrons. The emitted positron travels up to a few millimeters into the body and annihilates with an electron, which produces a pair of annihilation photons moving in opposite directions, both having an energy of 511 keV. The PET technique depends on the coincidental detection of the pair of photons 180° apart. Most currently used PET radionuclides have relatively short half-lifes: ^{11}C (20 min), ^{13}N (10 min), ^{15}O (2 min), ^{18}F (110 min) and ^{68}Ga (68 min). Alternative PET radionuclides having longer half-lifes such as ^{64}Cu (12.7 h), ^{76}Br (16.0 h), ^{86}Y (14.7 h), ^{89}Zr (78.4 h) and ^{124}I (4.2 h) are useful for labeling long-circulating molecules.

Radionuclide imaging can be used to assess the drug delivery vehicle's pharmacokinetic (PK) and pharmacodynamic (PD) properties. The DDS mainly works by altering the PK/PD properties of therapeutic agents. Therefore, it is critical to evaluate the PK/PD of free drugs and their deliverable formulations. Kleiter *et al.* [4] investigated Doxil® (Johnson & Johnson, Langhorne, PA) liposome (doxorubicin-containing thermosensitive liposomes) administrated concomitantly with ^{99m}Tc-labeled liposomes to estimate the effect of hyperthermia on intratumoral accumulation of doxorubicin in rat fibrosarcomas using SPECT. Hyperthermia increased intratumoral accumulation of ^{99m}Tc-labeled liposomes at 18 h post-treatment as compared with unheated controls. The tumor uptake of ^{99m}Tc-labeled liposomes showed significant positive correlation with intratumoral doxorubicin concentration ($r^2 = 0.92$) in both hyperthermic and unheated groups. Therefore, ^{99m}Tc-labeled liposome here served as a surrogate marker for Doxil delivery.

Radionuclide imaging can also be used to determine the number and density of a specific target, which is critical for successful targeted delivery of therapeutics. Some of the targeted drugs can be directly labeled with radioisotopes as theragnostics [5-7]. Integrin $\alpha v\beta 3$ is known to be upregulated in proliferating endothelial cells and a variety of cancer cells, which is associated with tumor metastasis, angiogenesis and prognosis. The integrin $\alpha v\beta 3$ expression level has been imaged by using radiolabeled antibodies [8], peptides [9-13] and peptidomimetics [14-17]. Abegrin (Vitaxin, MedImmune, Gaithersburg, MD) is a humanized monoclonal antibody against human integrin $\alpha v\beta 3$ currently in Phase II clinical trials. *In vivo* imaging using Abegrin-based probes is needed for better treatment monitoring and dose optimization. PET imaging showed that, in integrin $\alpha v\beta 3$ overexpressing U87MG tumor model, tumor uptake of ^{64}Cu-DOTA-Abegrin was as high as 49.4 ± 4.5 %ID/g at 71 h post-injection. Furthermore, ^{64}Cu-DOTA-Abegrin uptake in tumors correlated very well with $\alpha v\beta 3$ expression levels (U87MG > MDA-MB-435 ≈ PC3 > CL26) (**Figure 1A**) [8]. Consistent with the imaging results, ^{90}Y-DOTA-Abegrin significantly inhibited the growth of integrin $\alpha v\beta 3$ positive U87MG tumors, but showed little inhibitory effect on integrin $\alpha v\beta 3$ negative HT-29 tumors. RGD peptides have been utilized to deliver therapeutics [6,18,19] and radiolabeled for molecular imaging. For example, RGD-TNF fusion protein [6], when conjugated with DOTA and labeled with ^{64}Cu, showed similar binding affinity and cytotoxicity as compared with RGD-TNF protein. Similar to ^{64}Cu-DOTA-Abegrin, the uptake of ^{64}Cu-DOTA-RGD-TNF in tumors correlated very well with $\alpha v\beta 3$ expression levels (U87MG > MDA-MB-435 > C6). In addition, RGD-TNF showed a more potent anti-tumor effect in $\alpha v\beta 3$ positive MDA-MB-435 tumor model than TNF protein (**Figure 1B**). Peptidomimetics have been radiolabeled to image integrin $\alpha v\beta 3$ expression as well. RP748 is a integrin $\alpha v\beta 3$-specific small molecule [17]. It binds to activated integrin $\alpha v\beta 3$ with $K_d = 21 \pm 7$ nM in the presence of Mn^{2+}. ^{111}In-labeled RP748 was injected into apolipoprotein $E^{-/-}$ mice at different times after left carotid injury. Distribution of ^{111}In-RP748 was investigated by autoradiography and its relative intensity was at a maximum at 1 week and decreased by 4 weeks after injury, which correlated well with integrin $\alpha v\beta 3$ expression as assessed by immunohistochemical analysis. These findings will potentially lead to the development of non-invasive imaging strategies for vascular cell proliferation associated states, whether focal, as in post-angioplasty restenosis, or diffuse, as in pulmonary hypertension. As an extension of the successful application in integrin $\alpha v\beta 3$ imaging, PET imaging technique is expected to be used for imaging other important biomarkers, providing real-time functional information of disease behavior, such as biomarkers expression, vascular permeability and cell proliferation, which will allow for more accurate patient selection, monitoring and therapeutic intervention.

Using radiolabeled DDS to study the biodistribution, pharmacokinetic properties and therapeutic efficacy is non-invasive, highly sensitive and quantitative, which enables the determination of drug concentration in tissue. However, some intrinsic limitations of PET/SPECT imaging exist, such as low spatial resolution, which can be partially mitigated by SPECT-CT, PET-CT or PET-MRI fusion, which provides a correlation between the drug or tracer's concentration and anatomical structures. Another limitation of nuclear imaging is that radiolabeling may influence the properties of labeled compounds, especially in the case of short peptides and some bioactive proteins. To address this problem, the development of site-specific radiolabeling protocol is required.

2.2 Optically labeled drug delivery system

Optical fluorescence imaging is based on the interaction of visible and/or near-infrared light with tissue; it distinguishes itself from other imaging modalities by several key features. It provides high sensitivity for detection, it is non-radioactive and it allows repeated dosing, it is relatively inexpensive and it is generally easy to apply. In addition, it incorporates techniques ranging from subcellular microscopy to macroscopic photography and three-dimensional volumetric tomography [20,21]. A targeted fluorescent imaging probe is typically comprised of an affinity ligand recognizing a disease biomarker that is conjugated to an active optical reporter. The disease biomarker might be a specific protein, cell surface receptors or enzyme that is either expressed, or upregulated in cancer cells, or associated with underlying biological processes, such as angiogenesis and metastasis. The optical reporters include organic fluorophores and semiconductor quantum dots. The optical reporter can be either directly conjugated to the affinity ligand bound to the cancer biomarker, or indirectly attached via a linker segment to the affinity ligand. Other than fluorescent labels, the recently emerged Raman imaging probes will also be discussed here.

2.2.1 *DDS carrying fluorescent dyes*

Among the different technologies being used to image molecular events, near-infrared (NIR) fluorescent optical imaging is particularly promising. NIR light (650 – 900 nm) can penetrate to a depth of 5 – 10 mm in tissue owing to the low photon absorption by water and hemoglobin in this spectral range [22]. Trastuzumab is a humanized monoclonal antibody targeting the HER2/neu extracellular domain and has been approved for the treatment of patients with HER2/neu-overexpressing cancers [23]. Gee *et al.* [24] recently covalently modified trastuzumab with NIR dye cyanine 5.5 (Cy5.5). The trastuzumab–Cy5.5 conjugate was used to distinguish HER2-normal from HER2-overexpressing human breast tumors *in vitro* and *in vivo*. Serial *in vivo* tumor imaging studies revealed progressive accumulation of trastuzumab-Cy5.5 in HER2-overexpressing BT-474 and SKBR-3 tumors, an intermediate level of accumulation in MCF-7 tumors expressing HER-2 to some extent, but no accumulation in HER_2-negative 9L tumors. More importantly, trastuzumab-Cy5.5 enabled rapid interval assessment of the receptor level and adequate inhibition after therapy initiation. When BT-474 tumors were treated with saline, an intermediate dose of trastuzumab (5 mg/kg), or a full dose of trastuzumab (100 mg/kg), the binding of trastuzumab-AF750 to BT-474 tumor was either partially or almost completely blocked by 5 mg/kg and 100 mg/kg trastuzumab treatment, respectively. This study suggested practical applications of NIR imaging in the clinic, including non-invasive *in situ*

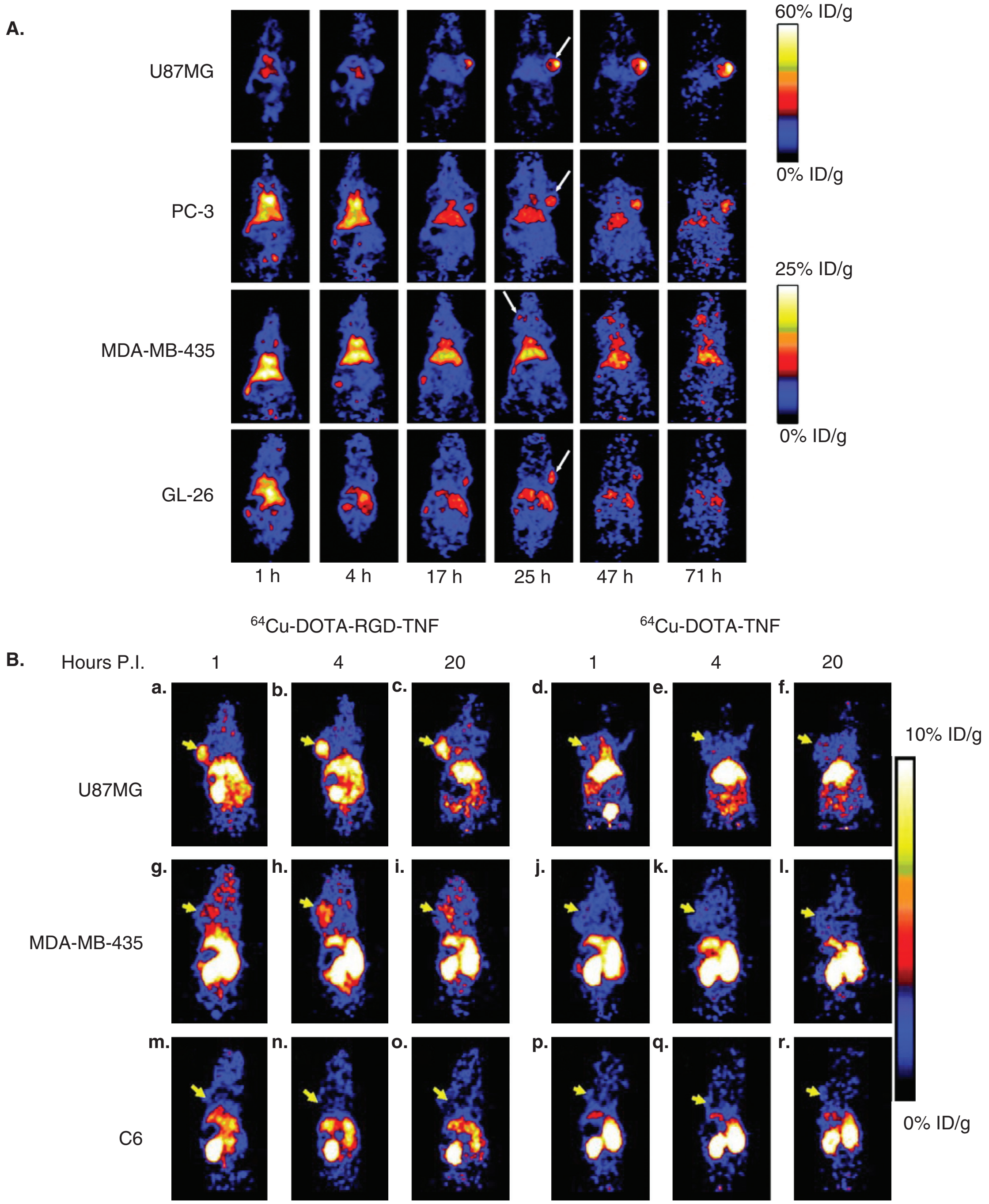

Figure 1. Positron emission tomography (PET) imaging probes coupled with targeted drug delivery potential. A. Serial microPET scans of mice bearing different tumors after injection of ^{64}Cu-DOTA-Abegrin. Note that ^{64}Cu-DOTA-Abegrin uptake in tumors correlated very well with $\alpha v\beta 3$ expression levels (U87MG>MDA-MB-435 = PC3 > CL26). **B.** Serial microPET studies of mice bearing different tumors after injection of ^{64}Cu-DOTA-RGD4C-TNF and ^{64}Cu-DOTA-TNF. Note that ^{64}Cu-DOTA-RGD4C-TNF uptake in tumors correlated very well with $\alpha v\beta 3$ expression levels (U87MG > MDA-MB-435 > C6).

1A reproduced with permission from American Association for Cancer Research from Cai W, Wu Y, Chen K, *et al.* *In vitro* and *in vivo* characterization of 64Cu-labeled Abegrin, a humanized monoclonal antibody against integrin alpha v beta 3. Cancer Res 2006;66:9673-81 [8]. Copyright © 2009 American Association for Cancer Research. 1B reproduced with permission from American Association for Cancer Research from Wang H, Chen K, Cai W, *et al.* Integrin-targeted imaging and therapy with RGD4C-TNF fusion protein. Mol Cancer Ther 2008;7:1044-53 [6]. Copyright © 2009 American Association for Cancer Research.

characterization of cancer patients, individualized drug dosing and imaging of primary therapeutic efficacy before changes in tumor growth are apparent. This strategy is generalizable to other monoclonal antibody cancer therapies and may be used to assess the adequacy of therapeutic dosing of the same antibody to block the target receptor.

2.2.2 DDS carrying semiconductor quantum dots

Semiconducting quantum dots (QDs) have emerged as a promising alternative to organic dyes as fluorescent biomarkers for *in vitro* and *in vivo* imaging; their superior brightness and photostability make them excellent candidates in the development of trackable multifunctional agents [25-30]. Detailed studies on the *in vivo* behaviors of QD probes revealed that QDs are delivered to tumors by both a passive targeting mechanism and an active targeting mechanism. In the passive mode, macromolecules and nanometer-sized particles are accumulated preferentially at tumor sites through the EPR effect [31]. Active targeting is usually achieved by conjugating to the QDs a targeting component that provides preferential accumulation of QDs in the tumor-bearing organ, in the tumor itself, individual cancer cells, or intracellular organelles inside cancer cells.

QDs can be engineered to carry targeting motif for biomarker imaging [32-38]. More desirably, QDs can be incorporated into a single nanoscale structure with tumor-targeting, imaging and drug delivery functions. Bagalkot *et al.* [39] reported a ternary novel system QD-Apt (Dox) composed of a QD, A10 RNA aptamer targeted to prostate-specific membrane antigen (PSMA) and the small molecular anticancer drug doxorubicin (Dox) for *in vitro* targeted imaging, therapy and sensing of drug release (**Figure 2A**). The QD-Apt (Dox) was able to deliver Dox to the targeted prostate cancer cells and sense the delivery of Dox by activating the fluorescence of QD, which concurrently images the cancer cells. Recently, Weng *et al.* [40] conjugated QD605/QD800 to Dox-loaded HER-2 targeted immunoliposomes (ILs). The Dox-loaded QD-ILs showed selective and efficient internalization, anticancer activity in HER-2 overexpressing tumor cells *in vitro*. Serial *in vivo* optical imaging showed that systematically administrated QD-ILs localized in HER2-overexpressing tumors. Although they did not test the antitumor effect of Dox-loaded QD-ILs *in vivo*, this is the first description of a targeted lipidic nanoparticle–QD system possessing tumor cell-targeting, imaging and drug delivery functions (**Figure 2B**).

QDs have also been used for RNA delivery and intracellular imaging. RNA interference (RNAi) is a powerful technology for sequence-specific suppression of genes and has broad applications ranging from functional gene analysis to targeted therapy. However, these applications are still limited by several major delivery problems in cellular entry, endosomal escape, dissociation from the carrier and coupling with cellular machine [41]. For cellular and *in vivo* RNAi deliveries, a number of approaches have been developed, which include QD-based small interfering RNA (siRNA) delivery and imaging. These QD probes are either mixed with conventional siRNA delivery agents [32] or external endosomal rupture compounds [42] for gene silencing activity. It is worth noting that by taking advantage of the versatile chemistry of polymer-encapsulated QDs, proton-sponge coated QDs [43] and QD–amphipol nanocomplex [44] were highly responsive to the acidic organelles and are suitable for siRNA binding and cell entry. As a result, the gene silencing efficiency was significantly improved and the cytotoxicity was reduced simultaneously.

However, tracking and quantification of QD *in vivo* by fluorescence imaging is limited by tissue absorption of light, which impairs excitation of QD in deeper lying tissues and decreases fluorescent light penetration from deeper structures to the surface, where it can be measured [45]. However, future innovations in optical imaging by novel measurement technology may be able to address this limitation, for example, by utilization of a high resolution *in vivo* 3D microscopic system [46] or utilizing photoacoustic (PA) properties of QDs to detect [47] both fluorescence light and PA waves by integrated PT-PA–fluorescence modalities. The latter advances will make *in vivo* studies of QDs pharmacokinetics in tissues and organs 2 – 3 cm depth possible.

2.2.3 DDS carrying photosensitizers

Photodynamic therapy (PDT) involves three key components: a photosensitizer, light and tissue oxygen. A photosensitizer is a chemical compound that can be excited by light of a specific wavelength [48-50]. This excitation uses visible or near-infrared light, and creates an excited singlet state oxygen molecule ($^1O_2$). Singlet oxygen is a very aggressive chemical species and will very rapidly react with any nearby biomolecules. Ultimately, these destructive reactions will kill cells through apoptosis or necrosis.

With increasing demand on treatment selectivity, the synergy of NIR fluorescence imaging and PDT is extremely compelling for several reasons. First, it is possible to use a single molecule for both purposes, since most photosensitizers can both emit fluorescence for NIRF imaging and produce cytotoxic reactive $^1O_2$ for PDT when activated by light. Second, the concentrations required for killing and imaging cells are in the same range and third, both techniques are promising *in vivo* cancer imaging and treatment modalities [51].

To improve the photosensitizer's tumor selectivity and specificity, many attempts have been made to direct photosensitizers to a known cellular target, including creating a photosensitizer conjugate with a ligand specific to the target [52-56]. A pyro-peptide-folate (PPF) construct [57], consisting of NIRF fluorophore and photosensitizer pyropheophorbide (Pyro), a stable peptide linker and modulator, and folate (**Figure 3A**), showed enhanced accumulation in folate receptor positive KB cancer cells both *in vitro* and *in vivo* (**Figure 3B**). Since most photosensitizers do not have the excitation and emission spectra favorable to image deep tissues, photosensitizers are sometimes coupled with NIR dyes for fluorescence image-guided PDT. A 'bifunctional agent' consisting of a highly effective photosensitizer, HPPH and a cyanine dye

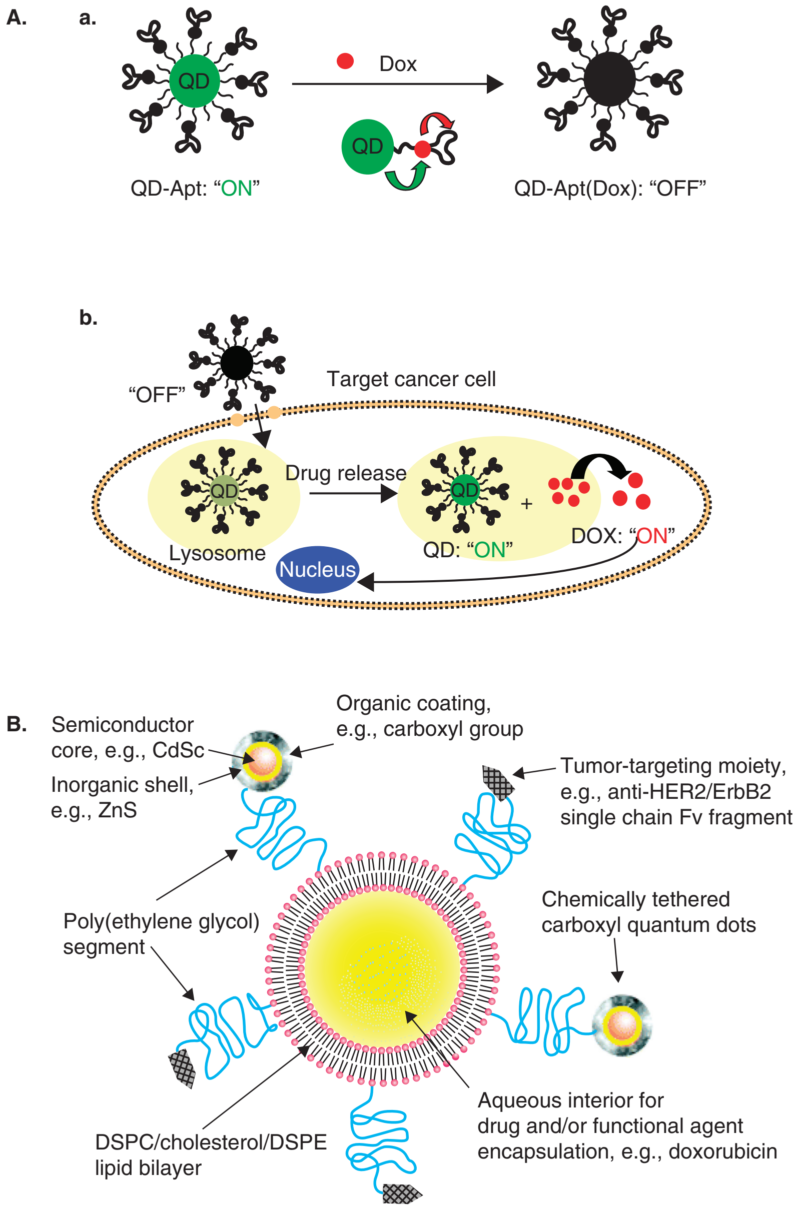

Figure 2. Optical imaging probes coupled with drug delivery potential. A. Schematic illustration of quantum dot (QD)–Apt (Dox) Bi-FRET system. (a) the CdSe/ZnS core-shell QD are surface functionalized with the A10 PSMA aptamer. The intercalation of Dox within the A10 PSMA aptamer on the surface of QDs results in the formation of the QD-Apt (Dox) and quenching of both QD and Dox fluorescence through a Bi-FRET mechanism resulting in the 'OFF' state. (b) Schematic illustration of specific uptake of QD-Apt (Dox) conjugates into target cancer cell through prostate-specific membrane antigen (PSMA) mediated endocytosis. The release of Dox from the QD-Apt (Dox) conjugates induces the recovery of fluorescence from QD and Dox ('ON' state), thereby sensing the intracellular delivery of Dox and enabling the synchronous fluorescent localization and killing of cancer cells. **B.** Schematic showing the structure of a QD-IL nanoparticle. Derivatized CdSe/ZnS core/shell QDs are represented as a sphere with a layer of organic coating (gray) covering the outer surface of the inorganic shell (yellow) and the semiconductor core (orange). Surface-derivatized QDs were chemically linked to functionalized PEG-DSPE incorporated in extruded liposomes. Anti-HER2 single chain Fv fragments (scFv, arrowheads) are attached to the end of PEG chains.

2A reproduced with permission from Bagalkot V, Zhang L, Levy-Nissenbaum E, *et al.* Quantum dot-aptamer conjugates for synchronous cancer imaging, therapy, and sensing of drug delivery based on bi-fluorescence resonance energy transfer. Nano Lett 2007;7:3065-70 [39]. Copyright © 2009 American Chemical Society.

2B reproduced with permission from Weng KC, Noble CO, Papahadjopoulos-Sternberg B, *et al.* Targeted tumor cell internalization and imaging of multifunctional quantum dot-conjugated immunoliposomes *in vitro* and *in vivo*. Nano Lett 2008;8:2851-7 [40]. Copyright © 2009 American Chemical Society.

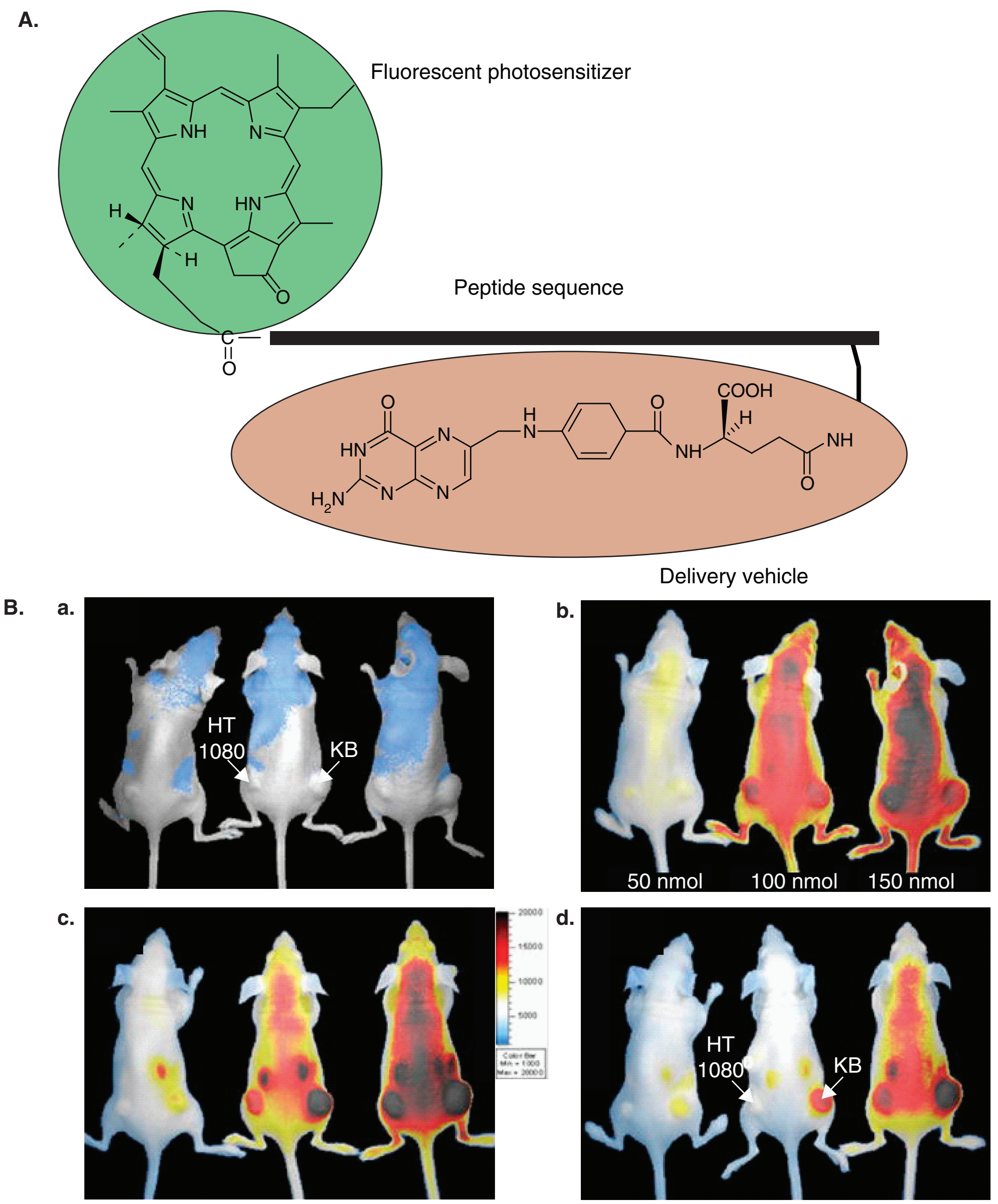

Figure 3. Fluorescent photosensitizer as an imaging and therapeutic agent. A. Pyro–GDEVDGSGK–Folate comprises three principal components: (1) fluorescent photosensitizer pyro-pheophorbide-a, an imaging and therapeutic agent; (2) peptide sequence, a stable and pharmacomodulating linker that can be exchanged with any organelle-targeting sequence; and (3) folate, serving as a cancer-specific delivery vehicle. **B.** Monitoring fluorescence signal distribution after i.v. injection of three different doses of pyro-peptide-folate (PPF) to double tumor-bearing mice that have a KB tumor (FR$^+$) on the right side and an HT 1080 tumor (FR–) on the left side, using a Xenogen imager. (a) Pre-scan, (b) 5 min after injection of 50 nmol (left mouse), 100 nmol (middle mouse) and 150 nmol (right mouse) of PPF, (c) 6 h after injection and (d) 24 h after injection. At this point, it is clear that PPF preferentially accumulates in the KB tumor. **C.** Structure of compound 5. **D.** *In vivo* photosensitizing efficacy of conjugate 5 in C3H mice (10 mice/group) bearing RIF tumors and variable concentrations. The tumors were exposed to a laser light (665 nm, 135 J/cm^2) at 24 h after injection. Drug concentrations were 0.5 – 2.5 µmol/kg (upper) and 2.5 – 3.5 µmol/kg (lower), respectively. **E.** High resolution tumor images indicated tumor localization of conjugate 5 in a live mouse 24 h after injection (drug dose = 0.3 µmol/kg). **F.** Schematic showing the structure of Fe_3O_4/SiO_2 (Ir) nanoparticles. i) 3-(Triethoxysilyl) propylisocyanate, THF, reflux; and ii) tetraethyl orthosilicate (TEOS) polymerization with addition of NH4OH under a reverse micelle system.

piq(H): 1-phenylisoquinoline; TES: triethoxysilane; NP: nanoparticle.

3A - B reproduced with permission from Stefflova K, Li H, Chen J, Zheng G. Peptide-based pharmacomodulation of a cancer-targeted optical imaging and photodynamic therapy agent. Bioconjug Chem 2007;18:379-88 [57]. Copyright © 2009 American Chemical Society.

3C - E reproduced with permission from Chen Y, Gryshuk A, Achilefu S, *et al.* A novel approach to a bifunctional photosensitizer for tumor imaging and phototherapy. Bioconjug Chem 2005;16:1264-74 [58] Copyright © 2009 American Chemical Society.

3F reproduced with permission from Lai CW, Wang YH, Lai CH, *et al.* Iridium-complex-functionalized Fe3O4/SiO2 core/shell nanoparticles: a facile three-in-one system in magnetic resonance imaging, luminescence imaging, and photodynamic therapy. Small 2008;4:218-24 [60]. Copyright © 2009 John Wiley & Sons Ltd..

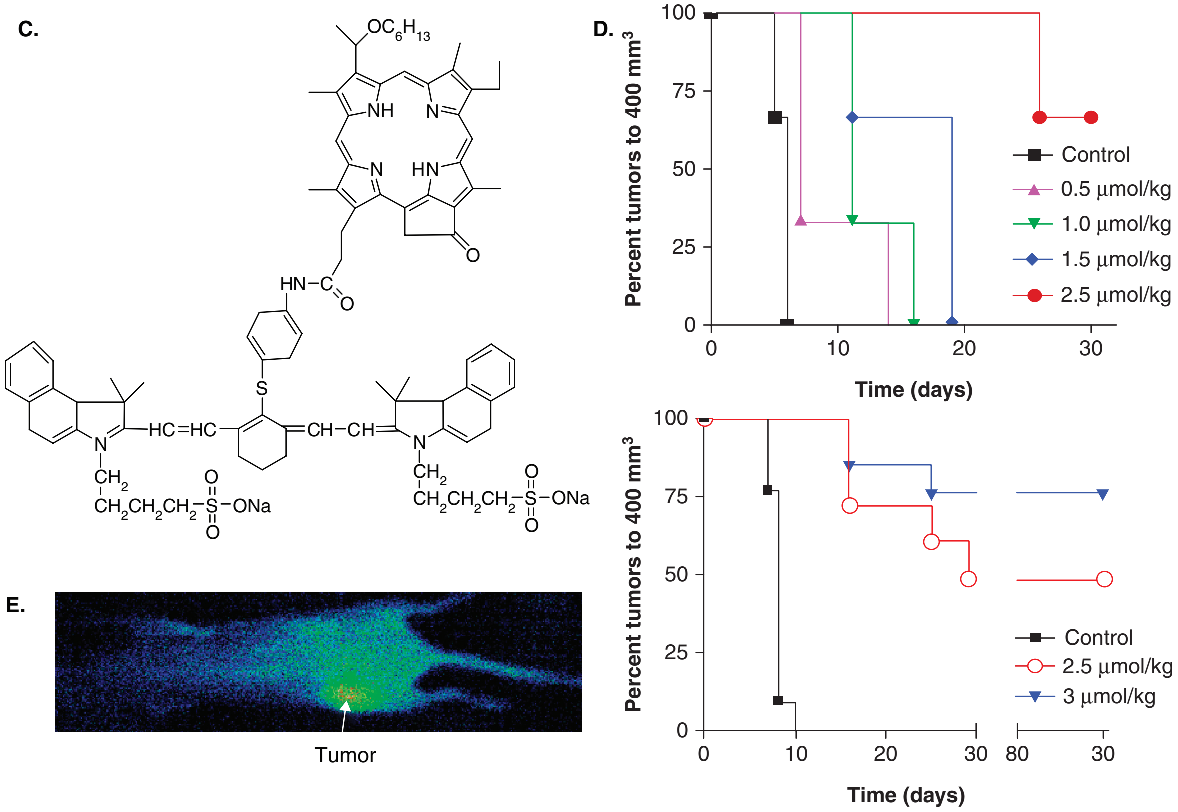

Figure 3. Fluorescent photosensitizer as an imaging and therapeutic agent (Continued). A. Pyro–GDEVDGSGK–Folate comprises three principal components: (1) fluorescent photosensitizer pyro-pheophorbide-a, an imaging and therapeutic agent; (2) peptide sequence, a stable and pharmacomodulating linker that can be exchanged with any organelle-targeting sequence; and (3) folate, serving as a cancer-specific delivery vehicle. **B.** Monitoring fluorescence signal distribution after i.v. injection of three different doses of pyro-peptide-folate (PPF) to double tumor-bearing mice that have a KB tumor (FR$^+$) on the right side and an HT 1080 tumor (FR–) on the left side, using a Xenogen imager. (a) Pre-scan, (b) 5 min after injection of 50 nmol (left mouse), 100 nmol (middle mouse) and 150 nmol (right mouse) of PPF, (c) 6 h after injection and (d) 24 h after injection. At this point, it is clear that PPF preferentially accumulates in the KB tumor. **C.** Structure of compound 5. **D.** *In vivo* photosensitizing efficacy of conjugate 5 in C3H mice (10 mice/group) bearing RIF tumors and variable concentrations. The tumors were exposed to a laser light (665 nm, 135 J/cm^2) at 24 h after injection. Drug concentrations were 0.5 – 2.5 µmol/kg (upper) and 2.5 – 3.5 µmol/kg (lower), respectively. **E.** High resolution tumor images indicated tumor localization of conjugate 5 in a live mouse 24 h after injection (drug dose = 0.3 µmol/kg). **F.** Schematic showing the structure of Fe_3O_4/SiO_2 (Ir) nanoparticles. i) 3-(Triethoxysilyl) propylisocyanate, THF, reflux; and ii) tetraethyl orthosilicate (TEOS) polymerization with addition of NH4OH under a reverse micelle system.

piq(H): 1-phenylisoquinoline; TES: triethoxysilane; NP: nanoparticle.

3A – B reproduced with permission from Stefflova K, Li H, Chen J, Zheng G. Peptide-based pharmacomodulation of a cancer-targeted optical imaging and photodynamic therapy agent. Bioconjug Chem 2007;18:379-88 [57]. Copyright © 2009 American Chemical Society.

3C – E reproduced with permission from Chen Y, Gryshuk A, Achilefu S, *et al.* A novel approach to a bifunctional photosensitizer for tumor imaging and phototherapy. Bioconjug Chem 2005;16:1264-74 [58]. Copyright © 2009 American Chemical Society.

3F reproduced with permission from Lai CW, Wang YH, Lai CH, *et al.* Iridium-complex-functionalized Fe3O4/SiO2 core/shell nanoparticles: a facile three-in-one system in magnetic resonance imaging, luminescence imaging, and photodynamic therapy. Small 2008;4:218-24 [60]. Copyright © 2009 John Wiley & Sons Ltd.

exhibiting long wavelength absorption at 660 and 836 nm, respectively, was designed and synthesized [58]. The resulting conjugate (**Figure 3C**) was found to localize in the mitochondria, the most sensitive intracellular target for PDT. The *in vivo* photosensitizing efficacy was determined by exposing tumor xenograft to light (135 J/cm^2) at 24 hr after injection of the conjugate at variable doses. As shown in **Figure 3D**, a clear dose–response relationship was observed, with a dose of 3.5 µmol/kg of the conjugate being highly effective in inhibiting tumor growth (80% mice were tumor-free at day 90). Whole body fluorescence imaging indicated significant tumor-imaging capability of the conjugate even at a dose of 0.3 µmol/kg, which was 10-fold less than the most effective therapeutic dose (**Figure 3E**). This approach provides a unique opportunity to develop more tumor-specific, bifunctional agents for tumor detection and therapy.

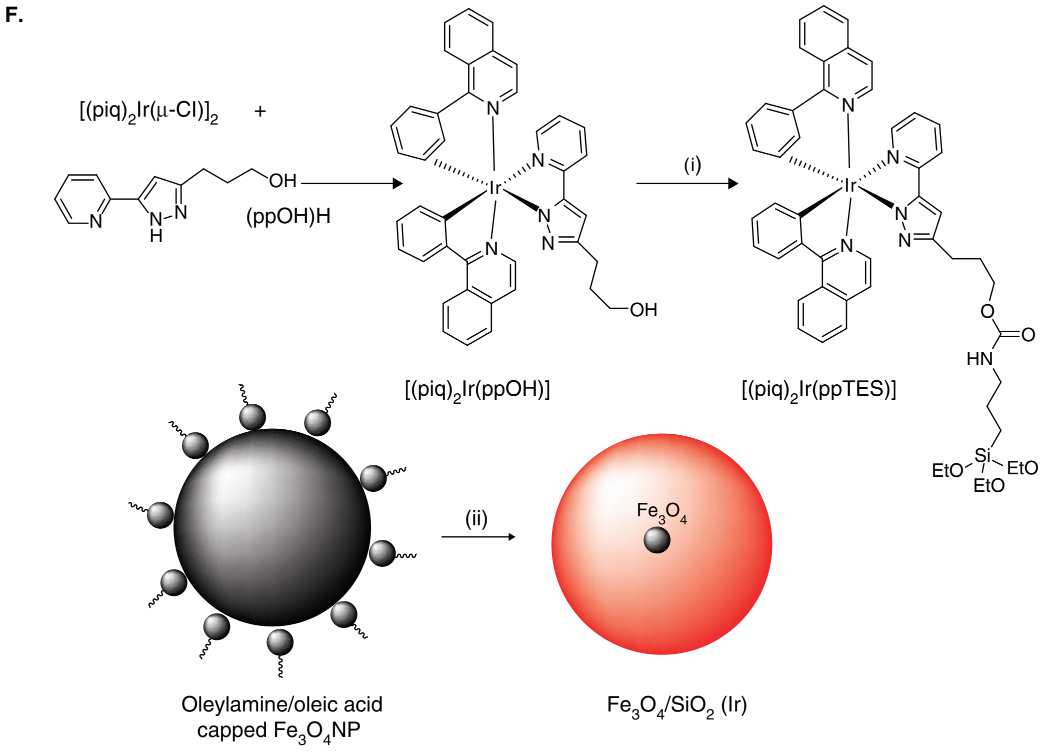

Figure 3. Fluorescent photosensitizer as an imaging and therapeutic agent (Continued). A. Pyro–GDEVDGSGK–Folate comprises three principal components: (1) fluorescent photosensitizer pyro-pheophorbide-a, an imaging and therapeutic agent; (2) peptide sequence, a stable and pharmacomodulating linker that can be exchanged with any organelle-targeting sequence; and (3) folate, serving as a cancer-specific delivery vehicle. **B.** Monitoring fluorescence signal distribution after i.v. injection of three different doses of pyro-peptide-folate (PPF) to double tumor-bearing mice that have a KB tumor (FR^+) on the right side and an HT 1080 tumor (FR–) on the left side, using a Xenogen imager. (a) Pre-scan, (b) 5 min after injection of 50 nmol (left mouse), 100 nmol (middle mouse) and 150 nmol (right mouse) of PPF, (c) 6 h after injection and (d) 24 h after injection. At this point, it is clear that PPF preferentially accumulates in the KB tumor. **C.** Structure of compound 5. **D.***In vivo* photosensitizing efficacy of conjugate 5 in C3H mice (10 mice/group) bearing RIF tumors and variable concentrations. The tumors were exposed to a laser light (665 nm, 135 J/cm^2) at 24 h after injection. Drug concentrations were 0.5 – 2.5 μmol/kg (upper) and 2.5 – 3.5 μmol/kg (lower), respectively. **E.** High resolution tumor images indicated tumor localization of conjugate 5 in a live mouse 24 h after injection (drug dose = 0.3 μmol/kg). **F.** Schematic showing the structure of Fe_3O_4/SiO_2 (Ir) nanoparticles. i) 3-(Triethoxysilyl) propylisocyanate, THF, reflux; and ii) tetraethyl orthosilicate (TEOS) polymerization with addition of NH4OH under a reverse micelle system.

piq(H): 1-phenylisoquinoline; TES: triethoxysilane; NP: nanoparticle.

3A – B reproduced with permission from Stefflova K, Li H, Chen J, Zheng G. Peptide-based pharmacomodulation of a cancer-targeted optical imaging and photodynamic therapy agent. Bioconjug Chem 2007;18:379-88 [57]. Copyright © 2009 American Chemical Society.

3C – E reproduced with permission from Chen Y, Gryshuk A, Achilefu S, *et al.* A novel approach to a bifunctional photosensitizer for tumor imaging and phototherapy. Bioconjug Chem 2005;16:1264-74 [58]. Copyright © 2009 American Chemical Society.

3F reproduced with permission from Lai CW, Wang YH, Lai CH, *et al.* Iridium-complex-functionalized Fe3O4/SiO2 core/shell nanoparticles: a facile three-in-one system in magnetic resonance imaging, luminescence imaging, and photodynamic therapy. Small 2008;4:218-24 [60]. Copyright © 2009 John Wiley & Sons Ltd.

To further improve the selectivity of PDT, Zheng *et al.* [59] introduced a concept of photodynamic molecular beacons (PMB) for controlling the photosensitizer's ability to generate $^1O_2$ and, ultimately, control its PDT activity. As we know that fluorescence resonance energy transfer (FRET)-based target activatable probes offer the control of fluorescence emission in response to specific cancer target; PDT is a cell-killing process by light activation of a photosensitizer in the presence of oxygen. The development of PMB is a combination of these two principles (FRET and PDT). It is comprised of a disease-specific linker, a photosensitizer and a $^1O_2$ quencher so that the photosensitizer's photoactivity is silenced until the linker interacts with a target molecule, such as a tumor-associated protease. As a proof-of-principle, an MMP-7-triggered PMB ($PP_{MMP7}B$) was synthesized using: i) pyro as photosensitizer because of its excellent $^1O_2$ quantum yield, NIR fluorescence emission and high tumor affinity; ii) black hole quencher 3 (BHQ3) as a dual fluorescence and $^1O_2$ quencher; and iii) a short peptide sequence, GPLGLARK, as the MMP7-cleavable linker. $PP_{MMP7}B$ showed MMP-7 specific production of $^1O_2$ free radicals, cell mitochondria specific uptake and photodynamic cytotoxicity in MMP-7 positive cells *in vitro*. After the $PP_{MMP7}B$ probe was intravenously injected into KB tumor-bearing mice, no fluorescent signal was observed initially, which confirmed that $PP_{MMP7}B$ is optically silent in its native state because of fluorescence quenching by BHQ3. However, the fluorescence signal started to increase in tumors 20 min after injection and reached the highest level at 3 hr afterwards, clearly indicating $PP_{MMP7}B$ activation by MMP-7. The PDT treatment was given at this time. Three days after PDT, the treated tumor in the drugged mouse reduced in size, and 30 days after PDT, it completely regressed without any sign of re-growth, whereas the untreated tumor and both tumors in the drug-free mouse continued to grow. These data demonstrate that $PP_{MMP7}B$ accumulates in MMP-7 positive tumors and can be photodynamically activated *in situ*.

To integrate MRI, luminescence imaging and PDT into a simple three-in-one functionality to avoid the side effect of systematic administered photosensitizer and to prevent luminescence quenching caused by direct contact of magnetic nanoparticles and dye molecules and consequent decrease of $^1O_2$ production from photosensitizer, Lai *et al.* [60] recently reported a new multifunctional system (**Figure 3F**) that consists of highly magnetized superparamagnetic iron oxide (SPIO) nanoparticles coated with an inorganic silica shell, which plays a key role in MRI, while the modified third-row transition-metal complexes encapsulated within SiO_2 serve dual functions as a photosensitizer and luminescent moiety. The Fe_3O_4/SiO_2(Ir) nanocomposite demonstrates its potential *in vitro* in multiple applications – the magnetic core provides the capability for MRI, the Ir^{3+} complex greatly enhances the spin-orbit coupling for phosphorescent labeling and simultaneous $^1O_2$ generation inducing apoptosis. But its *in vivo* application was hampered by its tendency to aggregate in high salt concentrations. Further optimization of surface modification is required.

2.2.4 DDS carrying Raman nanoparticles

The Raman effect is the inelastic scattering of the photon. When light is scattered from an atom or molecule, most photons are elastically scattered [61]. The scattered photons have the same frequency and wavelength as the incident photons. However, a small fraction of the scattered light (approximately 1 in 10^7 million photons) is inelastically scattered, with the scattered photons having a frequency different from, and usually lower than, the frequency of the incident photons. Raman spectroscopy can differentiate the spectral fingerprint of many molecules, resulting in very high multiple capabilities. Narrow spectral features are easily separated from the broad-band autofluorescence, and Raman active molecules are more photostable compared with fluorophores, which are rapidly photobleached. However, the inherently weak magnitude of the Raman effect limits the sensitivity and, as a result, the biomedical applications of Raman spectroscopy. The discovery of surface-enhanced Raman spectroscopy (SERS) overcomes this lack of sensitivity and has become a powerful tool for the characterization of a wide range of inorganic and biologically relevant analytes. The main advantage of SERS is a $10^3 – 10^7$ enhancement of the Raman signal of an analyte when it is adsorbed to or near the surface of nano-roughened noble metal, which results in high Raman intensities comparable to fluorescence. SERS Raman imaging is promising for the next generation of biological imaging (**Figure 4A – B**) [62].

A single walled nanotube (SWNT) is inherently Raman active and exhibits a strong Raman peak at 1,593 cm^{-1}. Various biological molecules like drugs [63-66], peptides [67], proteins [68], plasmid [69] and siRNA [70] have been incorporated onto SWNTs by either covalent coupling or non-covalent adsorption methods. The resulting solubilized nanotubes readily enter cells by endocytosis and by other mechanisms. Functionalized, solubilized SWNTs can cross cell membranes with little cytotoxicity. SWNTs also provide a very high surface area per unit weight for high drug loading. Lastly and foremost, the intrinsic spectroscopic properties of nanotubes, including Raman and photoluminescence, can provide valuable means of tracking, detecting and imaging SWNTs to understand the *in vivo* behavior and drug delivery efficacy *in vivo* [71]. Liu *et al.* [65] conjugated paclitaxel (PTX) to branched polyethylene glycol (PEG) chains on SWNTs via a cleavable ester bond to obtain a water soluble SWNT–PTX conjugate (**Figure 4A**). The i.v. injection of SWNT–PTX into tumor-bearing mice resulted in a tumor growth inhibition (TGI) of 59.4%, which was significantly more effective than the control formulations (**Figure 4B**). In addition, the intrinsic Raman scattering properties of SWNTs were utilized to determine the blood circulation half-life and biodistribution of SWNT–PTX by using Raman spectroscopy without relying on radiolabel or fluorescent label. SWNT–PTX conjugates showed high uptake in the reticulo-endothelial system (RES) organs, including the liver and spleen. Tumor uptake of SWNT–PTX increased significantly from ~ 1% ID/g at 30 min to ~ 5% ID/g at 2 h, indicating SWNT–PTX accumulation during this period through blood circulation. They further carried out micro-Raman imaging of SWNTs in tumor slices on sacrificed mice treated by SWNT–PTX at 24 hr after injection. The tumor uptake of SWNTs was indeed confirmed by Raman mapping of the SWNT characteristic G-band Raman peak in the tumor with a spatial resolution of ~ 1 µm.

Furthermore, SWNTs are semiconducting, quasi one-dimensional materials with small band-gaps in the order of ~ 1 eV, exhibiting photoluminescence in the NIR region [64,72]. NIR imaging of the photoluminescent SWNTs has been shown both *in vitro* and *in vivo* [73-75]. Antibodies conjugated SWNTs as near-infrared (NIR) fluorescent labels were able to successfully probe cell surface receptors with high specificity and high sensitivity (**Figure 4E – F**). The SWNT NIR fluorophores exhibit important advantages in low background, which could be used for sensitive molecular detection and imaging at the cellular level and eventually *in vivo*.

Despite all this promise, the biomedical applications of SWNT-based theragnostics are still in the exploratory stage. It is imperative to determine their toxicological and

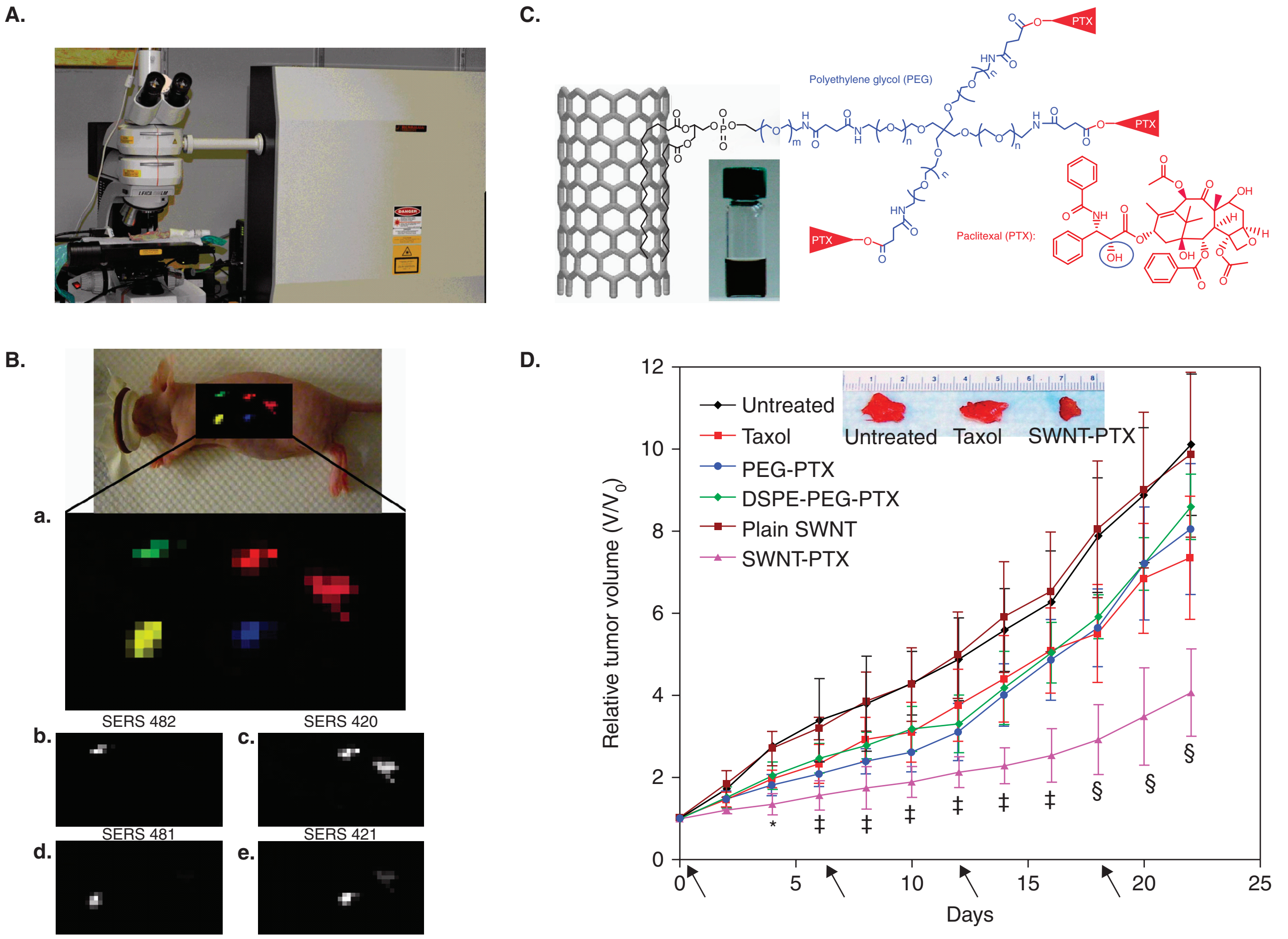

Figure 4. Single walled nanotubes (SWNTs) served as a targeted drug delivery vehicle and can be imaged by Raman spectroscopy. A. Photograph of Raman microscope adapted for small animal imaging with mouse positioned supine on an x–y translocation stage. **B.** Evaluation of multiplexing four different concentrations of SERS nanoparticles *in vivo*. (a) Raman map of four different surface-enhanced Raman spectroscopy (SERS) particles injected s.c. The fifth s.c. injection, represented in purple at the far right, is a mixture of the different four SERS particles with different concentrations. (b) Raman map depicting the SERS 482 nanoparticles; this injection site is green in (a). Notice how there is faint pixel brightness in the fifth injection site, corresponding to the least concentration of this SERS particle in the mixture. (c) Raman map depicting the SERS 420 nanoparticles; this injection site is red in (a). Note how there is intense pixel brightness in the fifth injection site corresponding to the highest concentration of this SERS particle in the mixture. (d) Raman map depicting SERS 481 nanoparticles; this injection site is yellow in (a). Notice how the fifth injection site shows the third brightest pixel intensity corresponding to the second least concentrated SERS particle mixture. (e) Raman map depicting the SERS 421 nanoparticles; this injection site is blue in (a). Notice how the fifth injection site shows the second brightest pixel intensity, corresponding to the second most concentrated of the SERS particle mixture. **C.** Schematic illustration of paclitaxel (PTX) conjugation to SWNT functionalized by phospholipids with branched PEG chains. **D.** Nanotube PTX delivery suppresses tumor growth of 4T1 breast cancer mice model. The tumor growth curves of 4T1 tumor-bearing mice that received different treatments are indicated. The same PTX dose (5 mg/kg) was injected (on days 0, 6, 12 and 18, marked by arrows) for Taxol, PEG-PTX, DSEP-PEG-PTX and SWNT–PTX. *$p < 0.05$; $^{\ddagger}p < 0.01$; $^{\S}p < 0.001$, Taxol versus SWNT–PTX. Inset, a photo of representative tumors taken out of an untreated mouse (left), a Taxol-treated mouse (middle) and a SWNT-PTX-treated mouse (right) after killing the mice at the end of the treatments. **E.** Near-infrared (NIR) fluorescence images of (a) Raji cells (B-cell lymphoma, CD20 positive) and (b) CEM cells (T-cell lymphoma, CD20 negative) treated with the SWNT–Rituxan conjugate. **F.** NIR fluorescence image of BT-474 cells (a), which are HER$_2$/neu positive, treated with the SWNT–Herceptin conjugate. NIR fluorescence image of MCF-7 cells (b), which are HER2/neu negative, treated with the SWNT–Herceptin conjugate.

4A – B reproduced with permission from Keren S, Zavaleta C, Cheng Z, *et al.* Noninvasive molecular imaging of small living subjects using Raman spectroscopy. Proc Natl Acad Sci USA 2008;105:5844-9 [62]. Copyright © 2009 National Academy of Sciences.

4C – D reproduced with permission from Liu Z, Chen K, Davis C, *et al.* Drug delivery with carbon nanotubes for in vivo cancer treatment. Cancer Res 2008;68:6652-60 [65]. Copyright © 2009 American Association for Cancer Research.

4E – F reproduced with permission from Welsher K, Liu Z, Daranciang D, Dai H. Selective probing and imaging of cells with single walled carbon nanotubes as near-infrared fluorescent molecules. Nano Lett 2008;8:586-90 [75]. Copyright © 2009 American Chemical Society.

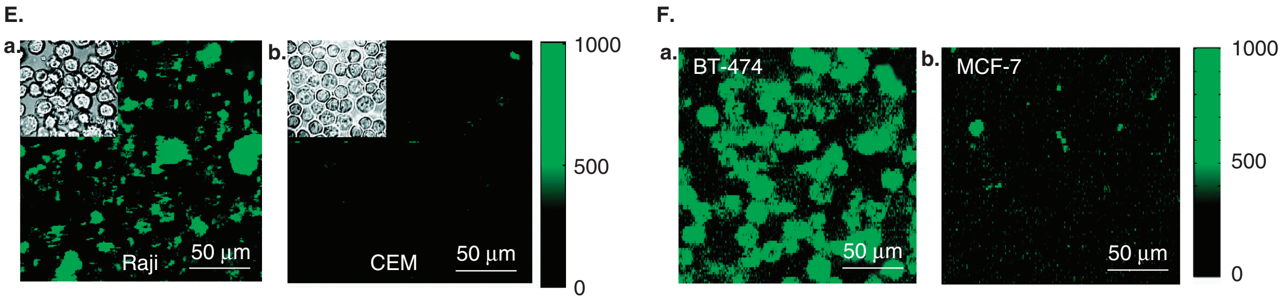

Figure 4. Single walled nanotubes (SWNTs) served as a targeted drug delivery vehicle and can be imaged by Raman spectroscopy (Continued). A. Photograph of Raman microscope adapted for small animal imaging with mouse positioned supine on an x–y translocation stage. **B.** Evaluation of multiplexing four different concentrations of SERS nanoparticles *in vivo*. (a) Raman map of four different surface-enhanced Raman spectroscopy (SERS) particles injected s.c. The fifth s.c. injection, represented in purple at the far right, is a mixture of the different four SERS particles with different concentrations. (b) Raman map depicting the SERS 482 nanoparticles; this injection site is green in (a). Notice how there is faint pixel brightness in the fifth injection site, corresponding to the least concentration of this SERS particle in the mixture. (c) Raman map depicting the SERS 420 nanoparticles; this injection site is red in (a). Note how there is intense pixel brightness in the fifth injection site corresponding to the highest concentration of this SERS particle in the mixture. (d) Raman map depicting SERS 481 nanoparticles; this injection site is yellow in (a). Notice how the fifth injection site shows the third brightest pixel intensity corresponding to the second least concentrated SERS particle mixture. (e) Raman map depicting the SERS 421 nanoparticles; this injection site is blue in (a). Notice how the fifth injection site shows the second brightest pixel intensity, corresponding to the second most concentrated of the SERS particle mixture. **C.** Schematic illustration of paclitaxel (PTX) conjugation to SWNT functionalized by phospholipids with branched PEG chains. **D.** Nanotube PTX delivery suppresses tumor growth of 4T1 breast cancer mice model. The tumor growth curves of 4T1 tumor-bearing mice that received different treatments are indicated. The same PTX dose (5 mg/kg) was injected (on days 0, 6, 12 and 18, marked by arrows) for Taxol, PEG-PTX, DSEP-PEG-PTX and SWNT–PTX. $^*p < 0.05$; $^‡p < 0.01$; $^§p < 0.001$, Taxol versus SWNT–PTX. Inset, a photo of representative tumors taken out of an untreated mouse (left), a Taxol-treated mouse (middle) and a SWNT-PTX-treated mouse (right) after killing the mice at the end of the treatments. **E.** Near-infrared (NIR) fluorescence images of (a) Raji cells (B-cell lymphoma, CD20 positive) and (b) CEM cells (T-cell lymphoma, CD20 negative) treated with the SWNT–Rituxan conjugate. **F.** NIR fluorescence image of BT-474 cells (a), which are HER$_2$/neu positive, treated with the SWNT–Herceptin conjugate. NIR fluorescence image of MCF-7 cells (b), which are HER2/neu negative, treated with the SWNT–Herceptin conjugate.

4A – B reproduced with permission from Keren S, Zavaleta C, Cheng Z, *et al.* Noninvasive molecular imaging of small living subjects using Raman spectroscopy. Proc Natl Acad Sci USA 2008;105:5844-9 [62]. Copyright © 2009 National Academy of Sciences.

4C – D reproduced with permission from Liu Z, Chen K, Davis C, *et al.* Drug delivery with carbon nanotubes for in vivo cancer treatment. Cancer Res 2008;68:6652-60 [65]. Copyright © 2009 American Association for Cancer Research.

4E – F reproduced with permission from Welsher K, Liu Z, Daranciang D, Dai H. Selective probing and imaging of cells with single walled carbon nanotubes as near-infrared fluorescent molecules. Nano Lett 2008;8:586-90 [75]. Copyright © 2009 American Chemical Society.

pharmacological profiles before any clinical application of carbon nanotubes can be deemed feasible. Recently, a number of studies have examined the toxicological profile of carbon nanotubes *in vivo*. Most of the carbon nanotubes cytotoxicity studies focused on pulmonary toxicity [76,77] and skin toxicity [78,79] after local administration. However, Singh *et al.* [80] reported that ^{111}In-DTPA-SWNT followed a rapid, first-order clearance from the blood compartment through the renal excretion route without any toxic side effects or mortality after i.v. injection. Their work presents for the first time the preliminary pharmacokinetic data of carbon nanotubes; further pharmacological investigations of different types of nanotubes are necessary to determine the limitations and opportunities that the non-biodegradable SWNT-based delivery system may offer.

2.3 Ultrasound contrast agent-based DDS

Ultrasonography (US) is by far the most commonly used clinical imaging modality worldwide because it is safe and cost effective. Ultrasonic contrast agents have been the subject of active research, especially in recent years, with added interest in developing site-directed ultrasonic contrast agents. A site-directed ultrasonic contrast agent is designed to specifically and sensitively enhance the acoustic reflectivity of a pathological tissue that would otherwise be difficult to distinguish from the surrounding normal tissue. Most site-targeted acoustic contrast agents are based on microbubbles [81] and nano-emulsions [82-84].

2.3.1 *Microbubbles*

Microbubbles are small (typically 1 – 4 µm in diameter) gas-filled bubbles used as ultrasound contrast agents [85,86], which work by resonating in an ultrasound beam, rapidly contracting and expanding in response to the pressure changes of the sound wave. By a fortunate coincidence, they vibrate particularly strongly at the high frequencies used for diagnostic ultrasound imaging, which makes them several thousand times more reflective than normal body tissues and consequently

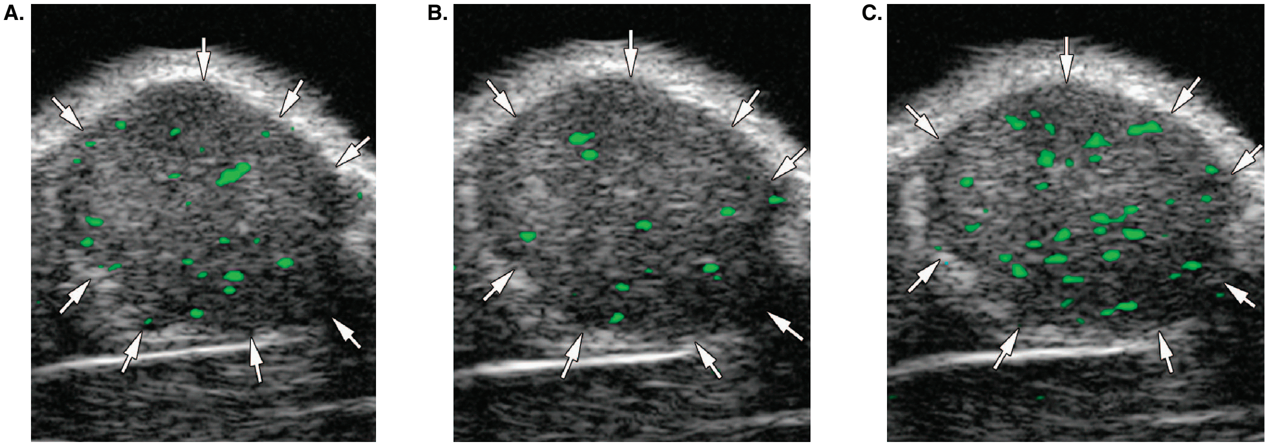

Figure 5. Microbubble-based ultrasound contrast agents coupled with drug delivery potential. A – C. Transverse color-coded ultrasound images in subcutaneous human ovarian adenocarcinoma (SK-OV-3) xenograft tumor (arrows) from nude mouse. Imaging was performed in same imaging session 4 min after i.v. injection of VEGFR-targeted microbubbles **A**, integrin αvβ3 targeted microbubbles, **B** or VEGFRs and integrin αvβ3 dual-targeted microbubbles **C**, with 30 min between injections to allow clearance of previously injected microbubbles.

Reproduced with permission from Willmann JK, Lutz AM, Paulmurugan R, *et al.* Dual-targeted contrast agent for US assessment of tumor angiogenesis *in vivo.* Radiology 2008;248:936-44 [99]. Copyright © 2009 Radiological Society of North America.

enhances both grey scale images and flow-mediated Doppler signals. Microbubble contrast agent was initially used as a blood pool contrast agent, allowing quantification of regional ischemia in the myocardium and other organs [87]; it can also be used to enhance imaging of the liver parenchyma [88-90] or to improve accuracy and sensitivity of cancer assessment or staging [91-93]. To broaden its application in the detection of a pathognomic molecular marker, site-targeted microbubbles have been developed to recognize thrombi [94], activated endothelial cells [95-97] and VEGFRs [98] to image molecular events *in vivo* and to assess inflammation, angiogenesis and early tumor detection. Willmann *et al.* [99] developed dual-targeted perfluorocarbon-filled microbubbles conjugated with anti-integrin αvβ3 and anti-VEGFR-2 antibodies (**Figure** 5A – C). However, the use of microbubbles in treatments may eventually be even more important than their diagnostic uses. Microbubbles can aid drug delivery in themselves by acting as 'cavitation nuclei' and as agents to carry drugs for site-specific treatment [100-102].

To facilitate drug delivery, microbubbles and drug are systematically injected simultaneously and circulate freely in small vessels [103,104]. Once a sufficiently strong ultrasound pulse is applied to the area, the microbubbles expand and rupture the endothelial lining. The drug is then able to extravasate. Recombinant VEGF [105] and rHGF [106] have been successfully delivered to the heart in a heart failure model using the ultrasound-targeted microbubble destruction method. The microbubbles can also be loaded with drugs [107,108]. In this case, the drug-laden microbubbles freely circulate throughout the vasculature. A pulse of ultrasound is applied and ruptures the microbubble, thereby liberating the drugs. Because ultrasound is applied locally, the drug is preferentially delivered locally. More desirably, microbubbles are modified with targeted motif and loaded with drugs as well for enhanced targeted drug delivery. Microbubbles with surface ligand and drug-laden are first freely circulated. Then the ligand preferentially binds to the endothelial target, resulting in an accumulation of microbubbles in the target region. An ultrasound pulse is then applied to liberate the drug. However, there is as yet no report on utilizing microbubbles equipped with both targeting ligand and therapeutic agents.

2.3.2 *Nano-emulsions*

Site-targeted nanoparticle contrast agents, when bound to the appropriate receptor, must be detected in the presence of bright echoes returned from the surrounding tissue. Targeted perfluorocarbon nanoparticles act as a suitable molecular imaging agent by modifying the acoustic impedance on the surface to which they bind [109]. Based on the well-described avidin–biotin interaction, target liquid-perfluorocarbon, lipid-encapsulated nanoparticles were delivered by a three-step strategy to fibrin expressed on clots [84,109]: the first step delivers a biotinylated antifibrin antibody; the second step delivers avidin; and lastly, biotinylated perfluorocarbon emulsion is delivered. Binding of site-targeted perfluorocarbon emulsion resulted in ultrasonic enhancement. Thrombi exposed to antifibrin-targeted contrast exhibited increased echogenicity. The enhancement showed monotonic increase with time for the targeted clots. In another study, Lanza *et al.* [82] prepared single-step perfluorocarbon emulsion, and conjugated the nano emulsion with F(ab)´ fragment against recombinant porcine tissue factor. Intravascular ultrasonic imaging was performed after targeted ultrasonic contrast injection in a stretch-induced tissue factor expression model in pigs. The results demonstrated that the targeted nanoparticles infiltrated the tunica media through the damaged endothelium and internal elastic lamina and bound to tissue factor epitopes expressed on myocyte membranes in response to the overstretch stimulus.

The favorable nature of ultrasound, such as its non-invasiveness, ease to control and most importantly the success of ultrasound-triggered local drug delivery via cavitation, radiation forces and/or heat convince us that in the near future, incorporation of both targeting motif and therapeutic motif (drugs, cytokine) to individual ultrasound contrast agents for focused ultrasound imaging and site-directed drug delivery using microbubbles, echogenic liposomes (ELIP) or liposomal bubbles [110-114], polymeric micelles [115-118] or a calcium carbonate suspension [119] are expected to extend the diagnostic and therapeutic horizons of ultrasound imaging greatly.

2.4 MRI imaging contrast agents coupled with drug delivery potential

Magnetic resonance imaging (MRI) is the most versatile and powerful imaging modality available in both clinical and research settings for visualizing soft tissues with high spatial resolution. MRI is based on the property that hydrogen protons align and process around an applied magnetic field, B_0. Upon application of a transverse radiofrequency pulse, these protons are perturbed from B_0. The subsequent process through which these protons return to their original state is referred to as the relaxation phenomenon. Two independent processes – longitudinal relaxation (T_1-recovery) and transverse relaxation (T_2-decay) – can be monitored to generate an MR image. The signal enhancement produced by MR contrast agents depends on their longitudinal or transverse relaxivity, which is defined as the ability of a contrast agent to shorten T_1 and T_2, that is r_1 ($1/T_1$) and r_2 ($1/T_2$), and is expressed in $mM^{-1}s^{-1}$. In general, there are two classes of MR contrast agents. The positive contrast agents, usually paramagnetic complex of Gd^{3+} or Mn^{2+} ions, have a low r_2/r_1 ratio and therefore generate positive contrast (bright/hot spots) in T_1-weighted images. Superparamagnetic contrast agents, have a high r_2/r_1 ratio and therefore cause dark spots in T_2- and T_2*-weighted images, and are therefore defined as negative contrast agents. These contrast agents are usually based on magnetic nanoparticles (MNPs), a class of nanoparticles commonly consisting of magnetic elements such as iron, nickle and cobalt and their chemical compounds.

So far, MRI contrast agents approved for clinical applications are mostly low molecular weight Gd^{3+} chelates, including Gd-DTPA, Gd-DOTA and their derivatives. However, these agents are rapidly extravasated from blood circulation and eliminated via renal clearance, which result in a transient time window for contrast-enhanced MRI examinations and a limited efficacy in improving MR image quality. As a result, several amphiphilic aggregates such as liposome, micelles, micro-emulsions and lipid proteins have been used as carriers to encapsulate Gd^{3+} or Mn^{2+} for MRI [120-124]. Here we will emphasize the recent progress on site-specific molecular imaging probes which can potentially aid in early disease detection, monitoring of treatment efficacy and drug development.

Targeted motifs can be directly attached to MR contrast agents, which include positive contrast agent, their derivatives and negative MR contrast agents, such as magnetic nanoparticles (MNP). These versatile targeted MR contrast agents have been used to image various biomarkers in various diseases and biological processes. Targeted contrast agents consisting of Gd-perfluorocarbon nanoparticles linked to the integrin $\alpha v\beta 3$ antibodies [125,126], RGD mimetics [127] or integrin $\alpha v\beta 3$ peptidomimetic antagonist [128,129] are able to enhance MR signal intensity in a integrin $\alpha v\beta 3$-dependent manner. For example, a thiolated peptidomimetic vitronectin antagonist (i.e., $\alpha v\beta 3$ antagonist) targeted paramagnetic nanoparticle was able to detect and characterize angiogenesis of nascent melanoma xenografts in nude mice bearing very small tumors (~ 30 mm^3) by increasing the spatial resolution and using a small surface coil [129]. MRI is a particularly sensitive modality to non-invasively visualize thromboses. High-resolution MRI detection and characterization of atherosclerotic lesions with serial imaging over time has been used to assess lesion progression or regression [130,131]. Flacke *et al.* [132] developed a novel fibrin-specific, lipid-encapsulated liquid perfluorocarbon nanoparticle that has high avidity, prolonged systemic half-life and can carry high Gd-DTPA payloads for high detection sensitivity. Imaged with 3D T1-weighted, fat-suppressed, fast-gradient-echo sequence, the fibrin-targeted paramagnetic nanoparticles showed great ability to enhance the detection of intravascular clots and minute thrombi within fissures of active vulnerable plaques. These studies demonstrated that high resolution MRI allows clinically relevant biomarkers to be detected and spatially localized.

Although it is highly possible to develop an MRI-visible, targeted nanoscale DDSs based on the Gd^{3+}-loaded macromolecules or MNPs, there are few reports regarding a single nanoscale system integrating both targeted imaging and targeted DDS so far. Nasongkla *et al.* [133] first described the development of multifunctional polymeric micelles composed of three key components: i) a chemotherapeutic agent Dox that is released from micelles through a pH-dependent mechanism; ii) a cyclic RGD ligand that can target integrin $\alpha v\beta 3$ on tumor endothelial cells; and iii) a cluster of SPIO nanoparticles loaded inside the hydrophobic core of each micelle for ultrasensitive MRI detection. The clustering of SPIO nanoparticles increased the T_2 relaxivity dramatically and as low as nanomolar concentration of SPIO–Dox micelles are MRI detectable due to the high loading density of SPIO (up to 50 w/w%). More specifically, at 6.25 Fe µg/ml, the MRI signal intensity decreased from 73.8 ± 7.0 for RGD-free micelles to 30.2 ± 3.5 for RGD-functionalized micelles (the untreated cells were used as a control with MR intensity at 100). In addition, the presence of the ionizable ammonium group on Dox ($pK_a \approx 7.0$) made the drug release pH-dependent. At pH 5.0, 10.4% of drug was released in 6 hr, approximately six times faster compared to

1.7% drug release at pH 7.4. The pH sensitivity facilitates drug release from micelles once inside the acidic endosomal compartment and increase the intracellular bioavailability of the drug. Hanessian *et al.* [134] covalently attached two well-known anti-tumor agents, 5-fluorouracil (5-FU) and Dox, to a mixed polymer of polyvinylalcohol (PVA) and poly(vinylalcohol/vinylamine) (aminoPVA) through appropriate bifunctional linkers, which upon enzyme cleavage released drugs at the target site, then the ferrofluid consisting of iron oxide nanoparticles were added to get the drug–SPION conjugates. The drug–SPION demonstrated highly synergistic anti-proliferative activity *in vitro* and superior T_2 relaxivity (r_2) and elongated circulation half-life *in vivo*. Lanza *et al.* [135] developed tissue-factor targeted nanoparticles containing Dox or PTX at 0, 0.2, or 2 mole% of the outer lipid layer. The nanoparticles were targeted for 30 min to tissue-factor positive vascular smooth muscle cells (VSMCs) and significantly inhibited the VSMCs proliferation in culture over the next 3 days. High-resolution T_1-weighted MRI at 4.7T demonstrated the targeted nanoparticles adherent to the VSMCs. Although the application of these drug-nanoparticles is limited to *in vitro* assays, this integrated nanomedicine platform opens many exciting opportunities for the targeted delivery of therapeutic agents as well as the use of MRI as a non-invasive strategy to monitor the treatment efficacy to improve the therapeutic outcome of drug therapy.

Very recently, Yu *et al.* [136] synthesized Dox-loaded thermally cross-linked SPIOs (TCL-SPIONs) (**Figure 6A**). The resulting Dox@TCL-SPIONs had a mean hydrodynamic size of 21 ± 6 nm and a narrow size distribution (PDI = 0.13). Dox@TCL-SPIONs showed superparamagnetic behavior with a saturation magnetization (Ms) of approximately 70 emu/g. Furthermore, the Dox released faster under the mildly acidic environment as a consequence of weakened binding between Dox and the partially neutralized carboxyl groups in TCL-SPION, with approximately 60% of the drug released from Dox@TCL-SPIONs at pH 5.1 in 50 min. To examine whether Dox@TCL-SPIONs are still able to localize and accumulate in tumors by EPR effect, MR imaging was performed. Before injection of Dox@TCL-SPIONs, the tumor appeared as a hyper-intense area in T_2-weighted MR images. At 4.5 h after Dox@TCL-SPIONs injection, noticeable darkening appeared in the tumor area with an RSE (relative signal enhancement) value of about 58%, indicating a large amount of Dox@TCL-SPIONs accumulated within the tumor (**Figure 6B**). To further examine the biodistribution of Dox in mice, Dox@TCL-SPIONs were injected into tumor-bearing mice. As we can see in **Figure 6C – E**, the fluorescence signal of Dox was clearly observed in the tumor at 1 hr after injection, which indicated fast accumulation and release of Dox; the fluorescence signal intensity increased over time and peaked at 12 hr post-injection. Besides, the fluorescence intensities in the liver were very weak in the case of Dox@TCL-SPIONs-injected mice relative to that of free Dox-injected mice, implying less liver toxicity with TCL-SPION DDS. More importantly, Dox@TCL-SPIONs (12.5 mg Fe/kg and 0.64 mg Dox/kg) showed superior anti-tumor effect than 5 mg/kg free Dox (**Figure 6F**) without showing any toxicity to major organs. These results indicated that Dox@TCL-SPIONs can efficiently reach the tumor site and then release drugs. Consequently, it is reasonable to anticipate that TCL-SPION may be utilized to develop combined therapeutic and diagnostic modalities.

2.5 DDS with multimodality imaging capabilities

As discussed above, each imaging modality has its own pros and cons, and a single technique does not necessarily possess all the required capabilities for comprehensive imaging. Therefore, multimodality imaging is becoming more common as a primary clinical tool for imaging human diseases, especially cancers. Structures containing multiple imaging modalities combined by CT, MRI, PET, SPECT, or optical have merit for potentially false-free sensing, multiparametric description of a disease process such as its location, extent, metabolic activity, blood flow and function of target tissue, resulting in better characterization of disease processes. However, the development of imaging agents for multimodality imaging is more challenging than single modality agents, requiring more complex design, multistep synthesis and careful selection of nuclear and optical tracers to avoid physical–chemical interference between molecular components. The integration of multicomponents, for example targeting motif, therapeutic agents and multimodal imaging labels (MRI/optical, PET/MRI, SPECT/MRI, PET/MRI/optical) into a single carrier, would be advantageous as it would require a single injection and exact colocalization of pathology based on two or more different parameters. By providing the imaging agents on the same vector, differences in the distribution of the agents would be minimized if not eliminated.

2.6 PET/optical dual modal imaging

The *in vivo* near-infrared fluorescence (NIFR) imaging has been mostly qualitative or at most semiquantitative. The development of dual-function PET/NIRF probe can allow for accurate assessment of the pharmocokinetics and tumor targeting efficacy of the probes, and additionally to aid the direct observation of probe location microscopically [38]. To assemble radioactive metal chelating agents and optical dyes into a single trifunctional (tumor targeting, nuclear imaging and optical imaging) agent for conjugation to antibodies, peptides, or other potential delivery vectors, Xu *et al.* [137] synthesized a chelator CHX-A'. Near-infrared dye Cy5.5 and a radiometal (^{86}Y(III) for PET, ^{111}In for SPECT) were introduced to the α-NH_2 and α-COOH of L-lysine, respectively, while the ε-NH_2 was used to introduce a maleimide moiety, thereby permitting conjugation of the CHX-A' to antibody trastuzumab. The resulting trastuzumab-^{111}In-Cy5.5 showed comparable immunoreactivity with native trastuzumab and may be used as a tumor-targeted monoclonal antibody probe for multimodality imaging. Although they did not test the antitumor effect of trastuzumab-^{111}In-Cy5.5 *in vivo*, the

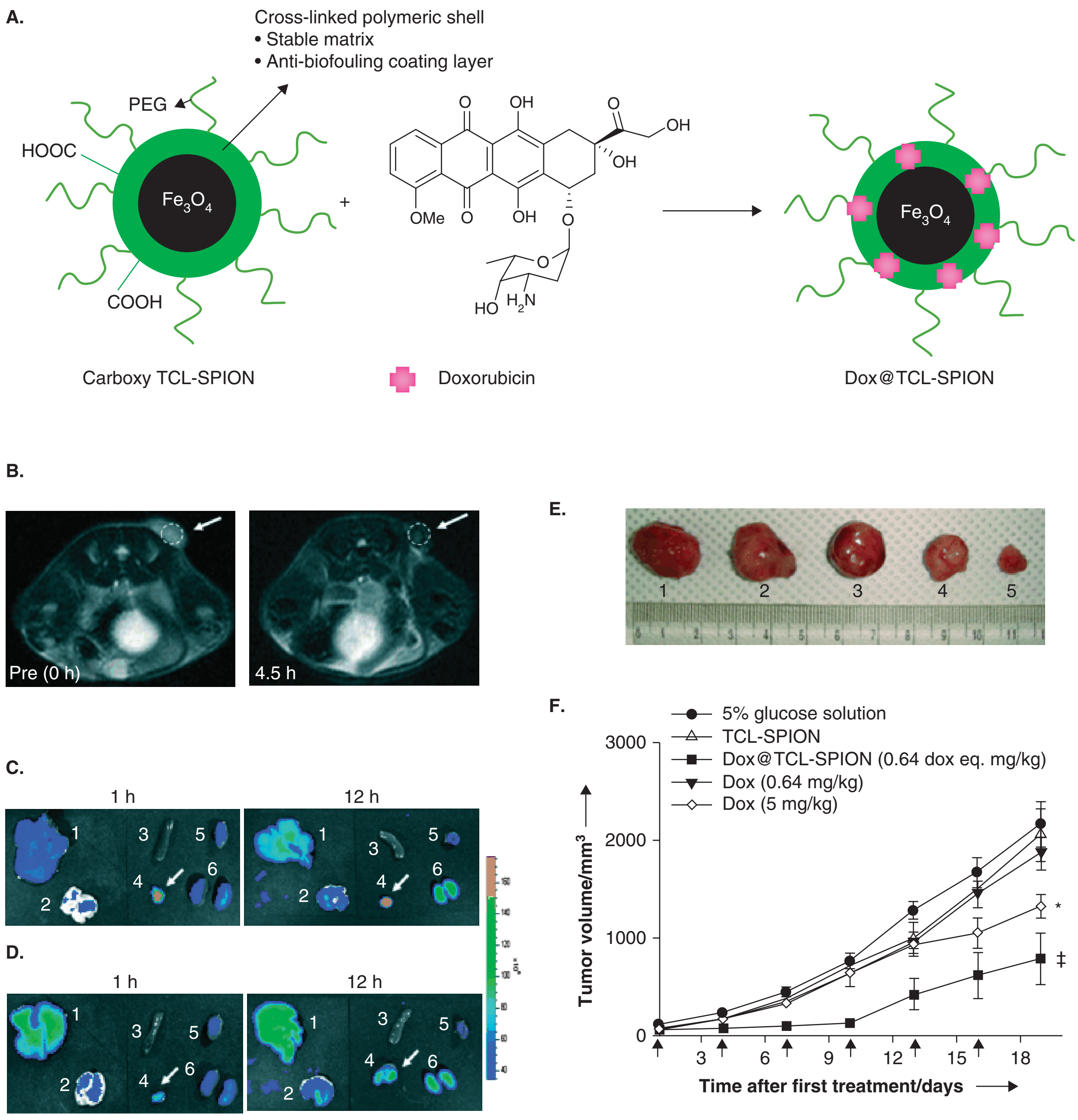

Figure 6. Magnetic resonance imaging (MRI) contrast agents coupled with targeted drug delivery potentials. A. Formation of Dox@TCL-SPIONs. **B.** T_2-weighted fast-spin echo images (time of repetition/time of echo: 4200 ms/102 ms) taken at 0 h and 4.5 h after injection of Dox@TCL-SPION at the level of LLC tumor on the right back of the mouse. The dashed circle with the white arrow indicates the allograft tumor region. **C – D.** Optical fluorescence images of major organs and allograft tumors: 1 liver; 2 lung; 3 spleen; 4 tumor; 5 heart; 6 kidney. Images were taken after i.v. injection of Dox@TCL-SPION (equivalent to 4 µg of Dox) C, and free Dox (4 µg) D, into tumor-bearing mice; mice were killed after 1 h and 12 h. Antitumor efficacy of Dox@TCL-SPION was tested in LLC allograft animal model. **E.** Excised tumors from mice euthanized after the 19th day of treatment with: 1 control; 2 TCL-SPION (12.5 mg Fe kg^{-1}); 3 Dox (0.64 mg kg^{-1}); 4 Dox (5 mg kg^{-1}); 5 Dox@TCL-SPION (12.5 mg Fe kg^{-1}, 0.64 mg Dox kg^{-1}). **F.** Tumor volume inhibition results from each treatment group ($*p < 0.005$, $^‡p < 0.01$, $n = 5 – 7$).

Reproduced with permission from Yu MK, Jeong YY, Park J, *et al.* Drug-loaded superparamagnetic iron oxide nanoparticles for combined cancer imaging and therapy *in vivo*. Angew Chem Int Ed Engl 2008;47:5362-5 [136]. Copyright © 2009 Wiley-VCH Verlag GmbH & Co. KGaA.

trastuzumab itself is a therapeutic agent used in the clinical setting, and furthermore, ^{111}In can be replaced by other radioisotopes, such as ^{90}Y and ^{177}Lu for immunoradiotherapy, therefore this strategy is applicable for clinical translation. Recently, a few examples of PET/NIRF dual modalities probe have been carried forward for investigation and evaluation *in vivo*. QD-based nanoprobe for dual PET and NIRF imaging of tumor VEGFR expression [138] and integrin αvβ3 expression [11], in which VEGF or RGD peptide is attached to amine-functionalized QD followed by DOTA conjugation for ^{64}Cu labeling. Both NIR fluorescence imaging and microPET demonstrated that ^{64}Cu-labeled DOTA-QD-VEGF and DOTA-QD-RGD primarily target the tumor vasculature through a specific ligand-receptor interaction.

2.7 MRI/optical dual modal imaging

Magnetic resonance imaging and optical techniques are highly complementary imaging methods. MRI/optical dual modal probes provide a macroscopic image with a ~ 50 μm spatial resolution by MR imaging, and *in vitro* fluorescent imaging can exhibit detailed microscopic information at the subcellular level. MRI contrast agent can be directly labeled with fluorescent dyes [139]. To prepare a dual modal imaging probe with therapeutic potential, a multifunctional nanoprobe [140] was synthesized, in which iron oxide nanoparticles were covalently coated with bifunctional poly(ethylene glycol) (PEG) polymers, and subsequently functionalized with chlorotoxin (Cltx), a glioma tumor-targeting molecule, and the near-infrared fluorescing (NIRF) molecule Cy5.5 (NPC-Cy5.5). NPC–Cy5.5 showed binding specificity to and increased internalization into glioma cells as demonstrated by MRI and confocal imaging. This multifunctional probe, although not tested *in vivo*, can be potentially applied for preoperative and postoperative diagnostic imaging with MRI and real-time intra-operative visualization of tumor margins. Saad *et al.* [141] equipped dendrimer with anticancer drug (paclitaxel), imaging agent (Cy5.5) and LHRP peptide targeted to receptors overexpressed on the cancer cell membrane as a tumor targeting moiety. Their results showed the specificity of the dendrimer nanoparticles for targeted cancer imaging with the prolonged clearance time and indicated the feasibility of incorporating both imaging probe and therapeutic agents in a single entity.

Several other strategies have been employed to develop robust and advanced MRI/optical probes. A core satellite nanoparticle probe comprised of a fluorescent dye-doped silica (DySiO2) core nanoparticle and multiple surrounding magnetic nanoparticles [142], fluorescent magnetic nanoparticles [143-146], or macromolecular carriers [147-154] with both MR contrast agents and fluorescence probes. These imaging probes can be functionalized for targeted imaging [155,156], but only a very limited number of reports have shown the incorporation of therapeutic agents into imaging probes. Cetuximab (Erbitux®, Elli Lilly, Indianapolis, IN; Bristol-Myers Squibb, New York, NY) is a chimeric monoclonal antibody, an epidermal growth factor receptor (EGFR) inhibitor, used in clinic for the treatment of metastatic colorectal cancer and head and neck cancer. Cetuximab was conjugated to spherical fluorescent magnetic nanohybrids (FMNHs) which consisted of $MnFe_2O_4$ magnetic nanocrystals encapsulated in pyrene-labeled poly(ε-caprolactone)-*b*-poly-(methacrylic acid) (PCL-b-PMAA). The resulting CET-FMNHs served as effective agents for both MR and fluorescence optical imaging of cancer cell lines [157], but its therapeutic efficacy was not tested. However, with the development of nanotechnology, the integrated capability of nanoscale MR and fluorescence imaging agents, along with their potential use as a drug delivery vehicle, these dual modality imaging agents may be coupled with therapeutics for future cancer diagnosis and therapy.

2.8 MRI/radionuclide imaging

MR contrast agents can be coupled with radionuclide labels for dual modal MRI/radionuclide imaging using a gamma camera, SPECT or PET. The combination of high resolution MRI and high sensitivity radionuclide imaging proved better spatial and anatomical information and also improved signal sensitivity [2]. To develop a bifunctional iron oxide nanoparticle probe for PET and MRI scans of tumor integrin αvβ3 expression, Lee *et al.* [13] synthesized polyaspartic acid (PASP)-coated IO (PASP-IO) nanoparticles as a T_2-weighted MRI contrast agent. Then the amine groups on PASP-IO were coupled with cyclic RGD peptides and DOTA chelators for PET after labeling with ^{64}Cu. DOTA-IO-RGD conjugates showed specific binding to integrin αvβ3-expressing cells *in vitro* and its r_2 and r_2* were measured to be 105.5 and 165.5 $s^{-1}mM^{-1}$, respectively. Both small animal PET and T_2-weighted MRI showed integrin-specific delivery of conjugated RGD-PASP-IO nanoparticles and prominent RES uptake. Choi *et al.* [158] also reported a magnetic nanoparticle-based PET/MRI probe. They first prepared MnMEIO with a composition of $MnFe_2O_4$, with measured T_2 relaxivity coefficient (r_2) of 321.6 $mM^{-1}s^{-1}$. The MnMEIO nanoparticle surface was exchanged with serum albumin (SA) to ensure high colloidal stability in a wide pH range and at high salt concentration. These SA–MnMEIO nanoparticles possess excellent nanoprobe characteristics with a monodispersed core size of 15 nm and a hydrodynamic size of 32 nm, including the SA coating. Then ^{124}I, a PET radionuclide, was directly conjugated to the tyrosine residue in SA. The ^{124}I-labeled SA-MnMEIO was injected subcutaneously into the right front paw of Sprague–Dawley rats. Dynamic PET images were taken for 1 hr; immediately followed by MR imaging at 1.5 T. Both brachial and auxiliary lymph nodes were clearly identified and accurately localized in a PET/MR fusion images as a result of the highly complementary nature of PET and MRI techniques. In both cases, the radioisotopes used for imaging can be replaced by ^{90}Y [13] or ^{131}I [158] for MRI-guided radiotherapy. In addition, the administration of αvβ3 targeted Gd-nanoparticles after SPECT/CT provided

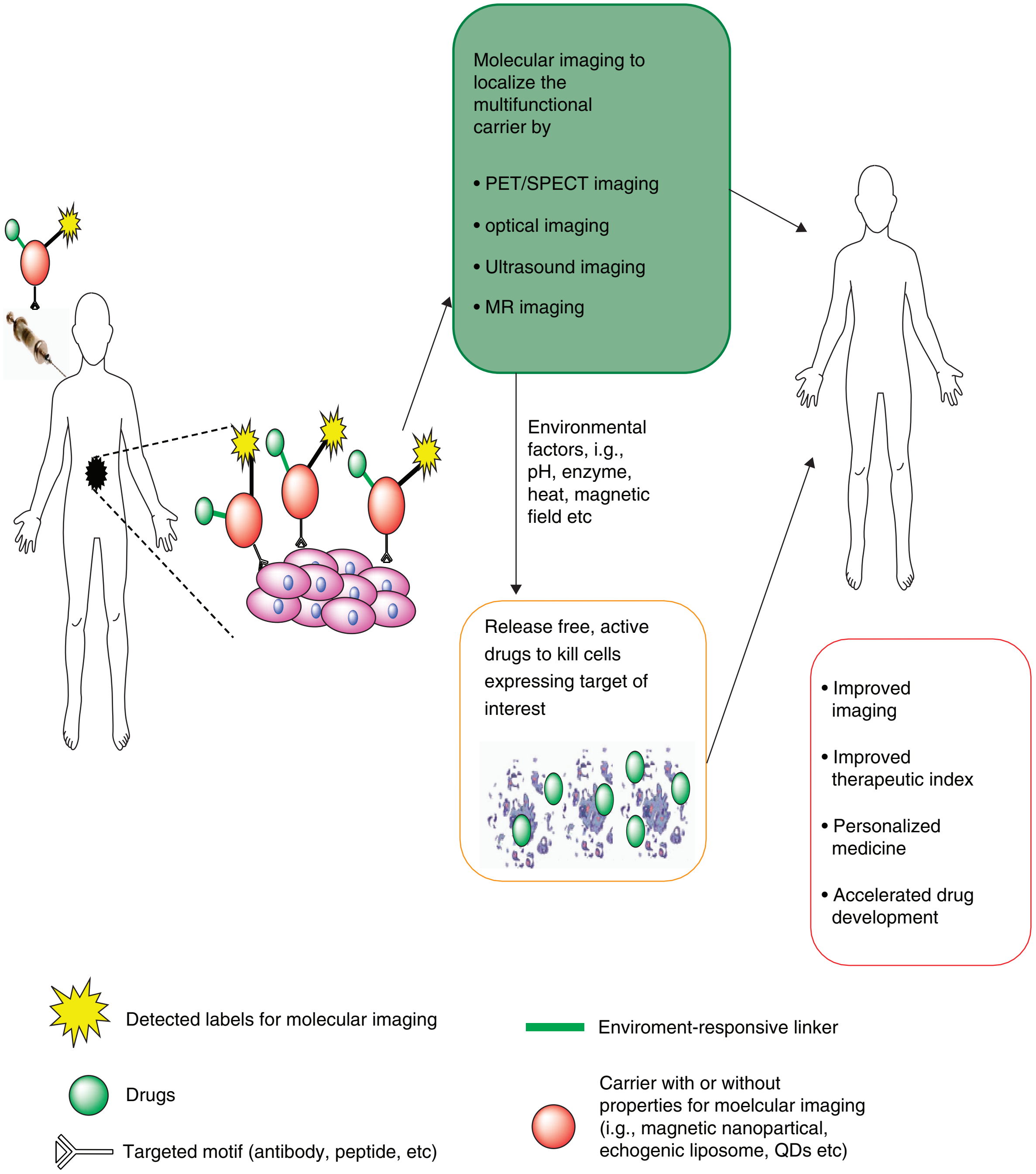

Figure 7. Development of an integrated system for simultaneous target imaging and drug delivery.

excellent MR detection of tumor angiogenesis and facilitated robust 3D characterization [2,3].

3. Conclusion

Thanks to various technological advancements and their integration, diverse types of targeted imaging probes coupled with drug delivery potential are now on the horizon (**Figure** 7). There have been only a limited number of single systems integrated with imaging and therapy property reported. However, preliminary data demonstrate promising potential for developing targeted carriers for simultaneous target imaging and drug delivery. Such an ideal system provides several advantages in the following aspects: i) it will contain a high payload of contrast-generating material, which greatly improves their detectability; ii) multiple properties may be easily integrated within one system to allow its detection with several imaging techniques and to include therapeutic qualities; and iii) the surface of such system may be modified to improve pharmacokinetic and pharmacodynamic properties by attaching targeting groups [159].

4. Expert opinion

Using a targeted theragnostic probe, we can see a specific molecular target in a living subject, following the distribution of a given drug in the same animal over time and quantification of the drug on the target, all in a non-invasive way. More desirably, triggerable drug delivery approaches can be incorporated together with targeted imaging probes within a single carrier. Such a highly versatile, multifunctional single carrier may provide attractive opportunities to combine the various imaging and therapeutic functions in quantities that will allow for accurate molecular imaging, targeted drug delivery and controlled release, as well as for strong therapeutic response. To fulfill this aim, strong collaborative efforts between imaging experts, pharmaceutical and biomedical scientists, and physicians are required.

The development of nanotechnology has a revolutionary impact on all areas of biomedicine, from research to diagnostics and therapeutics. Because of their size range, 10 – 100 nm, nanoparticles are very suitable for manipulation at the molecular level, for example cell–receptor binding for site-selective imaging and targeting, localization of encapsulated therapeutics for drug delivery. There are more than 100 nanosized particles containing anticancer agents in various stages of preclinical and clinical development. Current research interests include developing nanoscale therapeutics which can realize personalized medicine, new nanoparticles which can image structures deep inside the tissue and performing the dual function of treatment and imaging by adjusting the optical properties of nanoparticles, etc. Although progress has been slow, the development of targeted nanoscale carriers in which therapeutic and imaging agents are merged into a single system will certainly be of importance in the near future. Image-guided drug delivery using these multifunctional nanocarriers, containing targeted motif, therapeutic and imaging agents, will ultimately allow for real time monitoring of drug location, local concentration, targeting levels and drug release kinetics prior and during radio- and/or chemotherapeutic treatment.

Declaration of interest

The authors state no conflict of interest and have received no payment in the preparation of this manuscript.

Bibliography

1. Haberkorn U. PET and SPECT. Handb Exp Pharmacol 2008;(185 Pt 2):13-35
2. Hu G, Lijowski M, Zhang H, et al. Imaging of Vx-2 rabbit tumors with alpha(nu)beta3-integrin-targeted 111In nanoparticles. Int J Cancer 2007;120:1951-7
3. Lijowski M, Caruthers S, Hu G, et al. High sensitivity: high-resolution SPECT-CT/MR molecular imaging of angiogenesis in the Vx2 model. Invest Radiol 2009;44:15-22
4. Kleiter MM, Yu D, Mohammadian LA, et al. A tracer dose of technetium-99m-labeled liposomes can estimate the effect of hyperthermia on intratumoral doxil extravasation. Clin Cancer Res 2006;12:6800-7
5. Hsu AR, Cai W, Veeravagu A, et al. Multimodality molecular imaging of glioblastoma growth inhibition with vasculature-targeting fusion toxin VEGF121/rGel. J Nucl Med 2007;48:445-54
6. Wang H, Chen K, Cai W, et al. Integrin-targeted imaging and therapy with RGD4C-TNF fusion protein. Mol Cancer Ther 2008;7:1044-53
7. Cao Q, Cai W, Niu G, et al. Multimodality imaging of IL-18 – binding protein-Fc therapy of experimental lung metastasis. Clin Cancer Res 2008;14:6137-45
8. Cai W, Wu Y, Chen K, et al. In vitro and in vivo characterization of 64Cu-labeled Abegrin, a humanized monoclonal antibody against integrin alpha v beta 3. Cancer Res 2006;66:9673-81
9. Haubner R, Wester HJ, Burkhart F, et al. Glycosylated RGD-containing peptides: tracer for tumor targeting and angiogenesis imaging with improved biokinetics. J Nucl Med 2001;42:326-36
10. Haubner R, Wester HJ, Reuning U, et al. Radiolabeled alpha(v)beta3 integrin antagonists: a new class of tracers for tumor targeting. J Nucl Med 1999;40:1061-71
11. Cai W, Chen K, Li ZB, et al. Dual-function probe for PET and near-infrared fluorescence imaging of tumor vasculature. J Nucl Med 2007;48:1862-70
12. Hsu AR, Hou LC, Veeravagu A, et al. In vivo near-infrared fluorescence imaging of integrin alphavbeta3 in an orthotopic glioblastoma model. Mol Imaging Biol 2006;8:315-23
13. Lee HY, Li Z, Chen K, et al. PET/MRI dual-modality tumor imaging using arginine-glycine-aspartic (RGD)-conjugated radiolabeled iron oxide nanoparticles. J Nucl Med 2008;49:1371-9
14. Harris TD, Cheesman E, Harris AR, et al. Radiolabeled divalent peptidomimetic vitronectin receptor antagonists as potential tumor radiotherapeutic and imaging agents. Bioconjug Chem 2007;18:1266-79
15. Meoli DF, Sadeghi MM, Krassilnikova S, et al. Noninvasive imaging of myocardial angiogenesis following experimental myocardial infarction. J Clin Invest 2004;113:1684-91
16. Onthank DC, Liu S, Silva PJ, et al. 90Y and 111In complexes of a DOTA-conjugated integrin alpha v beta 3 receptor antagonist: different but biologically equivalent. Bioconjug Chem 2004;15:235-41
17. Sadeghi MM, Krassilnikova S, Zhang J, et al. Detection of injury-induced vascular remodeling by targeting activated alphavbeta3 integrin in vivo. Circulation 2004;110:84-90

18. Cao Q, Li ZB, Chen K, et al. Evaluation of biodistribution and anti-tumor effect of a dimeric RGD peptide-paclitaxel conjugate in mice with breast cancer. Eur J Nucl Med Mol Imaging 2008;35:1489-98
19. Alam MR, Dixit V, Kang H, et al. Intracellular delivery of an anionic antisense oligonucleotide via receptor-mediated endocytosis. Nucleic Acids Res 2008;36:2764-76
20. Giepmans BN, Adams SR, Ellisman MH, Tsien RY. The fluorescent toolbox for assessing protein location and function. Science 2006;312:217-24
21. Contag CH. In vivo pathology: seeing with molecular specificity and cellular resolution in the living body. Annu Rev Pathol 2007;2:277-305
22. Weissleder R. Molecular imaging in cancer. Science 2006;312:1168-71
23. Lewis GD, Figari I, Fendly B, et al. Differential responses of human tumor cell lines to anti-p185HER2 monoclonal antibodies. Cancer Immunol Immunother 1993;37:255-63
24. Gee MS, Upadhyay R, Bergquist H, et al. Human breast cancer tumor models: molecular imaging of drug susceptibility and dosing during HER2/neu-targeted therapy. Radiology 2008;248:925-35
25. Bruchez MP. Turning all the lights on: quantum dots in cellular assays. Curr Opin Chem Biol 2005;9:533-7
26. Jaiswal JK, Goldman ER, Mattoussi H, Simon SM. Use of quantum dots for live cell imaging. Nat Methods 2004;1:73-8
27. Jaiswal JK, Simon SM. Potentials and pitfalls of fluorescent quantum dots for biological imaging. Trends Cell Biol 2004;14:497-504
28. Medintz IL, Uyeda HT, Goldman ER, Mattoussi H. Quantum dot bioconjugates for imaging, labelling and sensing. Nat Mater 2005;4:435-46
29. Michalet X, Pinaud FF, Bentolila LA, et al. Quantum dots for live cells, in vivo imaging, and diagnostics. Science 2005;307:538-44
30. So MK, Xu C, Loening AM, et al. Self-illuminating quantum dot conjugates for in vivo imaging. Nat Biotechnol 2006;24:339-43
31. Duncan R. The dawning era of polymer therapeutics. Nat Rev Drug Discov 2003;2:347-60
32. Chen AA, Derfus AM, Khetani SR, Bhatia SN. Quantum dots to monitor RNAi delivery and improve gene silencing. Nucleic Acids Res 2005;33:e190
33. Gopalakrishnan G, Danelon C, Izewska P, et al. Multifunctional lipid/quantum dot hybrid nanocontainers for controlled targeting of live cells. Angew Chem Int Ed Engl 2006;45:5478-83
34. Tan WB, Jiang S, Zhang Y. Quantum-dot based nanoparticles for targeted silencing of HER2/neu gene via RNA interference. Biomaterials 2007;28:1565-71
35. Al-Jamal WT, Al-Jamal KT, Bomans PH, et al. Functionalized quantum dot–liposome hybrids as multimodal nanoparticles for cancer. Small 2008;4:1406-15
36. Gao X, Cui Y, Levenson RM, et al. In vivo cancer targeting and imaging with semiconductor quantum dots. Nat Biotechnol 2004;22:969-76
37. Kennel SJ, Woodward JD, Rondinone AJ, et al. The fate of MAb-targeted Cd(125m)Te/ZnS nanoparticles in vivo. Nucl Med Biol 2008;35:501-14
38. Schipper ML, Cheng Z, Lee SW, et al. microPET-based biodistribution of quantum dots in living mice. J Nucl Med 2007;48:1511-8
39. Bagalkot V, Zhang L, Levy-Nissenbaum E, et al. Quantum dot-aptamer conjugates for synchronous cancer imaging, therapy, and sensing of drug delivery based on bi-fluorescence resonance energy transfer. Nano Lett 2007;7:3065-70
40. Weng KC, Noble CO, Papahadjopoulos-Sternberg B, et al. Targeted tumor cell internalization and imaging of multifunctional quantum dot-conjugated immunoliposomes in vitro and in vivo. Nano Lett 2008;8:2851-7
41. Kim DH, Rossi JJ. Strategies for silencing human disease using RNA interference. Nat Rev Genet 2007;8:173-84
42. Derfus AM, Chen AA, Min DH, et al. Targeted quantum dot conjugates for siRNA delivery. Bioconjug Chem 2007;18:1391-6
43. Yezhelyev MV, Qi L, O'Regan RM, et al. Proton-sponge coated quantum dots for siRNA delivery and intracellular imaging. J Am Chem Soc 2008;130:9006-12
44. Qi L, Gao X. Quantum dot–amphipol nanocomplex for intracellular delivery and real-time imaging of siRNA. ACS Nano 2008;2:1403-10
45. Comsa DC, Farrell TJ, Patterson MS. Quantification of bioluminescence images of point source objects using diffusion theory models. Phys Med Biol 2006;51:3733-46
46. Takeda M, Tada H, Higuchi H, et al. In vivo single molecular imaging and sentinel node navigation by nanotechnology for molecular targeting drug delivery systems and tailor-made medicine. Breast Cancer 2008;15:145-52
47. Shashkov EV, Everts M, Galanzha EI, Zharov VP. Quantum dots as multimodal photoacoustic and photothermal contrast agents. Nano Lett 2008;8:3953-8
48. Chatterjee DK, Fong LS, Zhang Y. Nanoparticles in photodynamic therapy: an emerging paradigm. Adv Drug Deliv Rev 2008;60:1627-37
49. Donnelly RF, McCarron PA, Morrow DI, et al. Photosensitiser delivery for photodynamic therapy. Part 1: topical carrier platforms. Expert Opin Drug Deliv 2008;5:757-66
50. Donnelly RF, McCarron PA, Woolfson D. Drug delivery systems for photodynamic therapy. Recent Pat Drug Deliv Formul 2009;3:1-7
51. Stefflova K, Chen J, Zheng G. Killer beacons for combined cancer imaging and therapy. Curr Med Chem 2007;14:2110-25
52. Hemming AW, Davis NL, Dubois B, et al. Photodynamic therapy of squamous cell carcinoma. An evaluation of a new photosensitizing agent, benzoporphyrin derivative and new photoimmunoconjugate. Surg Oncol 1993;2:187-96
53. Schell C, Hombrecher HK. Synthesis and investigation of glycosylated mono- and diarylporphyrins for photodynamic therapy. Bioorg Med Chem 1999;7:1857-65
54. Schmidt-Erfurth U, Diddens H, Birngruber R, Hasan T. Photodynamic

targeting of human retinoblastoma cells using covalent low-density lipoprotein conjugates. Br J Cancer 1997;75:54-61

55. Vrouenraets MB, Visser GW, Stewart FA, et al. Development of meta-tetrahydroxyphenylchlorin-monoclonal antibody conjugates for photoimmunotherapy. Cancer Res 1999;59:1505-13
56. Vrouenraets MB, Visser GW, Stigter M, et al. Targeting of aluminum (III) phthalocyanine tetrasulfonate by use of internalizing monoclonal antibodies: improved efficacy in photodynamic therapy. Cancer Res 2001;61:1970-5
57. Stefflova K, Li H, Chen J, Zheng G. Peptide-based pharmacomodulation of a cancer-targeted optical imaging and photodynamic therapy agent. Bioconjug Chem 2007;18:379-88
58. Chen Y, Gryshuk A, Achilefu S, et al. A novel approach to a bifunctional photosensitizer for tumor imaging and phototherapy. Bioconjug Chem 2005;16:1264-74
59. Zheng G, Chen J, Stefflova K, et al. Photodynamic molecular beacon as an activatable photosensitizer based on protease-controlled singlet oxygen quenching and activation. Proc Natl Acad Sci USA 2007;104:8989-94
60. Lai CW, Wang YH, Lai CH, et al. Iridium-complex-functionalized Fe3O4/SiO2 core/shell nanoparticles: a facile three-in-one system in magnetic resonance imaging, luminescence imaging, and photodynamic therapy. Small 2008;4:218-24
61. Chourpa I, Lei FH, Dubois P, et al. Intracellular applications of analytical SERS spectroscopy and multispectral imaging. Chem Soc Rev 2008;37:993-1000
62. Keren S, Zavaleta C, Cheng Z, et al. Noninvasive molecular imaging of small living subjects using Raman spectroscopy. Proc Natl Acad Sci USA 2008;105:5844-9
63. Bianco A, Kostarelos K, Prato M. Applications of carbon nanotubes in drug delivery. Curr Opin Chem Biol 2005;9:674-9
64. Feazell RP, Nakayama-Ratchford N, Dai H, Lippard SJ. Soluble single-walled carbon nanotubes as longboat delivery systems for platinum(IV) anticancer drug design. J Am Chem Soc 2007;129:8438-9
65. Liu Z, Chen K, Davis C, et al. Drug delivery with carbon nanotubes for in vivo cancer treatment. Cancer Res 2008;68:6652-60
66. Bhirde AA, Patel V, Gavard J, et al. Targeted killing of cancer cells in vivo and in vitro with EGF-directed carbon nanotube-based drug delivery. ACS Nano 2009;3:307-16
67. Pantarotto D, Briand JP, Prato M, Bianco A. Translocation of bioactive peptides across cell membranes by carbon nanotubes. Chem Commun (Camb) 2004;16-7
68. Kam NW, Dai H. Carbon nanotubes as intracellular protein transporters: generality and biological functionality. J Am Chem Soc 2005;127:6021-6
69. Liu Y, Wu DC, Zhang WD, et al. Polyethylenimine-grafted multiwalled carbon nanotubes for secure noncovalent immobilization and efficient delivery of DNA. Angew Chem Int Ed Engl 2005;44:4782-5
70. Kam NW, Liu Z, Dai H. Functionalization of carbon nanotubes via cleavable disulfide bonds for efficient intracellular delivery of siRNA and potent gene silencing. J Am Chem Soc 2005;127:12492-3
71. Liu Z, Cai W, He L, et al. In vivo biodistribution and highly efficient tumour targeting of carbon nanotubes in mice. Nat Nanotechnol 2007;2:47-52
72. Kam NW, O'Connell M, Wisdom JA, Dai H. Carbon nanotubes as multifunctional biological transporters and near-infrared agents for selective cancer cell destruction. Proc Natl Acad Sci USA 2005;102:11600-5
73. Cherukuri P, Bachilo SM, Litovsky SH, Weisman RB. Near-infrared fluorescence microscopy of single-walled carbon nanotubes in phagocytic cells. J Am Chem Soc 2004;126:15638-9
74. Cherukuri P, Gannon CJ, Leeuw TK, et al. Mammalian pharmacokinetics of carbon nanotubes using intrinsic near-infrared fluorescence. Proc Natl Acad Sci USA 2006;103:18882-6
75. Welsher K, Liu Z, Daranciang D, Dai H. Selective probing and imaging of cells with single walled carbon nanotubes as near-infrared fluorescent molecules. Nano Lett 2008;8:586-90
76. Warheit DB, Laurence BR, Reed KL, et al. Comparative pulmonary toxicity assessment of single-wall carbon nanotubes in rats. Toxicol Sci 2004;77:117-25
77. Lam CW, James JT, McCluskey R, Hunter RL. Pulmonary toxicity of single-wall carbon nanotubes in mice 7 and 90 days after intratracheal instillation. Toxicol Sci 2004;77:126-34
78. Maynard AD, Baron PA, Foley M, et al. Exposure to carbon nanotube material: aerosol release during the handling of unrefined single-walled carbon nanotube material. J Toxicol Environ Health A 2004;67:87-107
79. Yokoyama A, Sato Y, Nodasaka Y, et al. Biological behavior of hat-stacked carbon nanofibers in the subcutaneous tissue in rats. Nano Lett 2005;5:157-61
80. Singh R, Pantarotto D, Lacerda L, et al. Tissue biodistribution and blood clearance rates of intravenously administered carbon nanotube radiotracers. Proc Natl Acad Sci USA 2006;103:3357-62
81. Mayer CR, Geis NA, Katus HA, Bekeredjian R. Ultrasound targeted microbubble destruction for drug and gene delivery. Expert Opin Drug Deliv 2008;5:1121-38
82. Lanza GM, Abendschein DR, Hall CS, et al. Molecular imaging of stretch-induced tissue factor expression in carotid arteries with intravascular ultrasound. Invest Radiol 2000;35:227-34
83. Lanza GM, Trousil RL, Wallace KD, et al. In vitro characterization of a novel, tissue-targeted ultrasonic contrast system with acoustic microscopy. J Acoust Soc Am 1998;104:3665-72
84. Lanza GM, Wallace KD, Scott MJ, et al. A novel site-targeted ultrasonic contrast agent with broad biomedical application. Circulation 1996;94:3334-40
85. Ladam-Marcus V, Mac G, Job L, et al. Contrast-enhanced ultrasound and liver imaging: review of the literature. J Radiol 2009;90:93-108
86. Qin S, Caskey CF, Ferrara KW. Ultrasound contrast microbubbles in imaging and therapy: physical principles and engineering. Phys Med Biol 2009;54:R27-57
87. Porter TR, Cwajg J. Myocardial contrast echocardiography: a new gold standard for perfusion imaging? Echocardiography 2001;18:79-87

88. Nakano H, Ishida Y, Hatakeyama T, et al. Contrast-enhanced intraoperative ultrasonography equipped with late Kupffer-phase image obtained by sonazoid in patients with colorectal liver metastases. World J Gastroenterol 2008;14:3207-11
89. Oldenburg A, Albrecht T. Baseline and contrast-enhanced ultrasound of the liver in tumor patients. Ultraschall Med 2008;29:488-98
90. Watanabe R, Matsumura M, Munemasa T, et al. Mechanism of hepatic parenchyma-specific contrast of microbubble-based contrast agent for ultrasonography: microscopic studies in rat liver. Invest Radiol 2007;42:643-51
91. Lee DJ, Lyshchik A, Huamani J, et al. Relationship between retention of a vascular endothelial growth factor receptor 2 (VEGFR2)-targeted ultrasonographic contrast agent and the level of VEGFR2 expression in an in vivo breast cancer model. J Ultrasound Med 2008;27:855-66
92. Palmowski M, Huppert J, Hauff P, et al. Vessel fractions in tumor xenografts depicted by flow- or contrast-sensitive three-dimensional high-frequency Doppler ultrasound respond differently to antiangiogenic treatment. Cancer Res 2008;68:7042-9
93. Rossi F, Leone VF, Vignoli M, et al. Use of contrast-enhanced ultrasound for characterization of focal splenic lesions. Vet Radiol Ultrasound 2008;49:154-64
94. Wang B, Wang L, Zhou XB, et al. Thrombolysis effect of a novel targeted microbubble with low-frequency ultrasound in vivo. Thromb Haemost 2008;100:356-61
95. Takalkar AM, Klibanov AL, Rychak JJ, et al. Binding and detachment dynamics of microbubbles targeted to P-selectin under controlled shear flow. J Control Release 2004;96:473-82
96. Ottoboni S, Short RE, Kerby MB, et al. Characterization of the in vitro adherence behavior of ultrasound responsive double-shelled microspheres targeted to cellular adhesion molecules. Contrast Media Mol Imaging 2006;1:279-90
97. Ellegala DB, Leong-Poi H, Carpenter JE, et al. Imaging tumor angiogenesis with contrast ultrasound and microbubbles targeted to alpha(v)beta3. Circulation 2003;108:336-41
98. Willmann JK, Cheng Z, Davis C, et al. Targeted microbubbles for imaging tumor angiogenesis: assessment of whole-body biodistribution with dynamic micro-PET in mice. Radiology 2008;249:212-9
99. Willmann JK, Lutz AM, Paulmurugan R, et al. Dual-targeted contrast agent for US assessment of tumor angiogenesis in vivo. Radiology 2008;248:936-44
100. Lindner JR. Microbubbles in medical imaging: current applications and future directions. Nat Rev Drug Discov 2004;3:527-32
101. Keller MW, Segal SS, Kaul S, Duling B. The behavior of sonicated albumin microbubbles within the microcirculation: a basis for their use during myocardial contrast echocardiography. Circ Res 1989;65:458-67
102. Lindner JR, Ismail S, Spotnitz WD, et al. Albumin microbubble persistence during myocardial contrast echocardiography is associated with microvascular endothelial glycocalyx damage. Circulation 1998;98:2187-94
103. Miller DL, Quddus J. Diagnostic ultrasound activation of contrast agent gas bodies induces capillary rupture in mice. Proc Natl Acad Sci USA 2000;97:10179-84
104. Price RJ, Skyba DM, Kaul S, Skalak TC. Delivery of colloidal particles and red blood cells to tissue through microvessel ruptures created by targeted microbubble destruction with ultrasound. Circulation 1998;98:1264-7
105. Mukherjee D, Wong J, Griffin B, et al. Ten-fold augmentation of endothelial uptake of vascular endothelial growth factor with ultrasound after systemic administration. J Am Coll Cardiol 2000;35:1678-86
106. Iwasaki M, Adachi Y, Nishiue T, et al. Hepatocyte growth factor delivered by ultrasound-mediated destruction of microbubbles induces proliferation of cardiomyocytes and amelioration of left ventricular contractile function in Doxorubicin-induced cardiomyopathy. Stem Cells 2005;23:1589-97
107. Chen S, Ding JH, Bekeredjian R, et al. Efficient gene delivery to pancreatic islets with ultrasonic microbubble destruction technology. Proc Natl Acad Sci USA 2006;103:8469-74
108. Hauff P, Seemann S, Reszka R, et al. Evaluation of gas-filled microparticles and sonoporation as gene delivery system: feasibility study in rodent tumor models. Radiology 2005;236:572-8
109. Hall CS, Marsh JN, Scott MJ, et al. Time evolution of enhanced ultrasonic reflection using a fibrin-targeted nanoparticulate contrast agent. J Acoust Soc Am 2000;108:3049-57
110. Klegerman ME, Zou Y, McPherson DD. Fibrin targeting of echogenic liposomes with inactivated tissue plasminogen activator. J Liposome Res 2008;18:95-112
111. Negishi Y, Endo Y, Fukuyama T, et al. Delivery of siRNA into the cytoplasm by liposomal bubbles and ultrasound. J Control Release 2008;132:124-30
112. Huang SL, McPherson DD, Macdonald RC. A method to co-encapsulate gas and drugs in liposomes for ultrasound-controlled drug delivery. Ultrasound Med Biol 2008;34:1272-80
113. Kee PH, Abruzzo TA, Smith DA, et al. Synthesis, acoustic stability, and pharmacologic activities of papaverine-loaded echogenic liposomes for ultrasound controlled drug delivery. J Liposome Res 2008;18:263-77
114. Xi X, Yang F, Chen D, et al. A targeting drug-delivery model via interactions among cells and liposomes under ultrasonic excitation. Phys Med Biol 2008;53:3251-65
115. Kik K, Lwow F, Szmigiero L. Polymeric drug carriers activated by ultrasounds energy. Polim Med 2007;37:59-65
116. Steinberg Y, Schroeder A, Talmon Y, et al. Triggered release of aqueous content from liposome-derived sol-gel nanocapsules. Langmuir 2007;23:12024-31
117. Husseini GA, Diaz de la Rosa MA, Gabuji T, et al. Release of doxorubicin from unstabilized and stabilized micelles under the action of ultrasound. J Nanosci Nanotechnol 2007;7:1028-33
118. Zeng Y, Pitt WG. A polymeric micelle system with a hydrolysable segment for drug delivery. J Biomater Sci Polym Ed 2006;17:591-604
119. Lanting B, Barfett J. Encapsulated calcium carbonate suspensions: a drug delivery vehicle sensitive to ultrasound disruption. Mcgill J Med 2006;9:108-10
120. Mulder WJ, Strijkers GJ, van Tilborg GA, et al. Lipid-based nanoparticles for

contrast-enhanced MRI and molecular imaging. NMR Biomed 2006;19:142-64

121. Torchilin VP. PEG-based micelles as carriers of contrast agents for different imaging modalities. Adv Drug Deliv Rev 2002;54:235-52

122. Dear JW, Kobayashi H, Brechbiel MW, Star RA. Imaging acute renal failure with polyamine dendrimer-based MRI contrast agents. Nephron Clin Pract 2006;103:c45-9

123. Kobayashi H, Brechbiel MW. Dendrimer-based nanosized MRI contrast agents. Curr Pharm Biotechnol 2004;5:539-49

124. Maeda H, Seymour LW, Miyamoto Y. Conjugates of anticancer agents and polymers: advantages of macromolecular therapeutics in vivo. Bioconjug Chem 1992;3:351-62

125. Anderson SA, Rader RK, Westlin WF, et al. Magnetic resonance contrast enhancement of neovasculature with alpha(v)beta(3)-targeted nanoparticles. Magn Reson Med 2000;44:433-9

126. Sipkins DA, Cheresh DA, Kazemi MR, et al. Detection of tumor angiogenesis in vivo by alphaVbeta3-targeted magnetic resonance imaging. Nat Med 1998;4:623-6

127. Winter PM, Morawski AM, Caruthers SD, et al. Molecular imaging of angiogenesis in early-stage atherosclerosis with alpha(v) beta3-integrin-targeted nanoparticles. Circulation 2003;108:2270-4

128. Winter PM, Caruthers SD, Kassner A, et al. Molecular imaging of angiogenesis in nascent Vx-2 rabbit tumors using a novel alpha(nu)beta3-targeted nanoparticle and 1.5 tesla magnetic resonance imaging. Cancer Res 2003;63:5838-43

129. Schmieder AH, Winter PM, Caruthers SD, et al. Molecular MR imaging of melanoma angiogenesis with alphanubeta3-targeted paramagnetic nanoparticles. Magn Reson Med 2005;53:621-7

130. Toussaint JF, LaMuraglia GM, Southern JF, et al. Magnetic resonance images lipid, fibrous, calcified, hemorrhagic, and thrombotic components of human atherosclerosis in vivo. Circulation 1996;94:932-8

131. Skinner MP, Yuan C, Mitsumori L, et al. Serial magnetic resonance imaging of experimental atherosclerosis detects lesion fine structure, progression and complications in vivo. Nat Med 1995;1:69-73

132. Flacke S, Fischer S, Scott MJ, et al. Novel MRI contrast agent for molecular imaging of fibrin: implications for detecting vulnerable plaques. Circulation 2001;104:1280-5

133. Nasongkla N, Bey E, Ren J, et al. Multifunctional polymeric micelles as cancer-targeted, MRI-ultrasensitive DDSs. Nano Lett 2006;6:2427-30

134. Hanessian S, Grzyb JA, Cengelli F, Juillerat-Jeanneret L. Synthesis of chemically functionalized superparamagnetic nanoparticles as delivery vectors for chemotherapeutic drugs. Bioorg Med Chem 2008;16:2921-31

135. Lanza GM, Yu X, Winter PM, et al. Targeted antiproliferative drug delivery to vascular smooth muscle cells with a magnetic resonance imaging nanoparticle contrast agent: implications for rational therapy of restenosis. Circulation 2002;106:2842-7

136. Yu MK, Jeong YY, Park J, et al. Drug-loaded superparamagnetic iron oxide nanoparticles for combined cancer imaging and therapy in vivo. Angew Chem Int Ed Engl 2008;47:5362-5

137. Xu H, Baidoo K, Gunn AJ, et al. Design, synthesis, and characterization of a dual modality positron emission tomography and fluorescence imaging agent for monoclonal antibody tumor-targeted imaging. J Med Chem 2007;50:4759-65

138. Chen K, Li ZB, Wang H, et al. Dual-modality optical and positron emission tomography imaging of vascular endothelial growth factor receptor on tumor vasculature using quantum dots. Eur J Nucl Med Mol Imaging 2008;35:2235-44

139. Kircher MF, Mahmood U, King RS, et al. A multimodal nanoparticle for preoperative magnetic resonance imaging and intraoperative optical brain tumor delineation. Cancer Res 2003;63:8122-5

140. Veiseh O, Sun C, Gunn J, et al. Optical and MRI multifunctional nanoprobe for targeting gliomas. Nano Lett 2005;5:1003-8

141. Saad M, Garbuzenko OB, Ber E, et al. Receptor targeted polymers, dendrimers, liposomes: which nanocarrier is the most efficient for tumor-specific treatment and imaging? J Control Release 2008;130:107-14

142. Lee JH, Jun YW, Yeon SI, et al. Dual-mode nanoparticle probes for high-performance magnetic resonance and fluorescence imaging of neuroblastoma. Angew Chem Int Ed Engl 2006;45:8160-2

143. Bakalova R, Zhelev Z, Aoki I, et al. Multimodal silica-shelled quantum dots: direct intracellular delivery, photosensitization, toxic, and microcirculation effects. Bioconjug Chem 2008;19:1135-42

144. Bakalova R, Zhelev Z, Aoki I, et al. Silica-shelled single quantum dot micelles as imaging probes with dual or multimodality. Anal Chem 2006;78:5925-32

145. Magana D, Perera SC, Harter AG, et al. Switching-on superparamagnetism in Mn/CdSe quantum dots. J Am Chem Soc 2006;128:2931-9

146. van Tilborg GA, Mulder WJ, Chin PT, et al. Annexin A5-conjugated quantum dots with a paramagnetic lipidic coating for the multimodal detection of apoptotic cells. Bioconjug Chem 2006;17:865-8

147. Baleizao C, Nagl S, Schaferling M, et al. Dual fluorescence sensor for trace oxygen and temperature with unmatched range and sensitivity. Anal Chem 2008;80:6449-57

148. Chen JW, Pham W, Weissleder R, Bogdanov A Jr. Human myeloperoxidase: a potential target for molecular MR imaging in atherosclerosis. Magn Reson Med 2004;52:1021-8

149. Hafez IM, Ansell S, Cullis PR. Tunable pH-sensitive liposomes composed of mixtures of cationic and anionic lipids. Biophys J 2000;79:1438-46

150. Hafez IM, Cullis PR. Tunable pH-sensitive liposomes. Methods Enzymol 2004;387:113-34

151. Karagianis G, Reiss JA, Marchesini R, et al. Biophysical and biological evaluation of porphyrin–bisacridine conjugates. Anticancer Drug Des 1996;11:205-20

152. Pikkemaat JA, Wegh RT, Lamerichs R, et al. Dendritic PARACEST contrast agents for magnetic resonance imaging. Contrast Media Mol Imaging 2007;2:229-39

153. Traitel T, Goldbart R, Kost J. Smart polymers for responsive drug delivery systems. J Biomater Sci Polym Ed 2008;19:755-67

154. Viglianti BL, Abraham SA, Michelich CR, et al. In vivo monitoring of tissue pharmacokinetics of liposome/drug using MRI: illustration of targeted delivery. Magn Reson Med 2004;51:1153-62

155. Mulder WJ, Koole R, Brandwijk RJ, et al. Quantum dots with a paramagnetic coating as a bimodal molecular imaging probe. Nano Lett 2006;6:1-6

156. Oostendorp M, Douma K, Hackeng TM, et al. Quantitative molecular magnetic resonance imaging of tumor angiogenesis using cNGR-labeled paramagnetic quantum dots. Cancer Res 2008;68:7676-83

157. Yang J, Lim EK, Lee HJ, et al. Fluorescent magnetic nanohybrids as multimodal imaging agents for human epithelial cancer detection. Biomaterials 2008;29:2548-55

158. Choi JS, Park JC, Nah H, et al. A hybrid nanoparticle probe for dual-modality positron emission tomography and magnetic resonance imaging. Angew Chem Int Ed Engl 2008;47:6259-62

159. Mulder WJ, Griffioen AW, Strijkers GJ, et al. Magnetic and fluorescent nanoparticles for multimodality imaging. Nanomed 2007;2:307-24

Affiliation

Hui Wang PhD & Xiaoyuan Chen† PhD
†Author for correspondence
Stanford University School of Medicine,
The Molecular Imaging Program at Stanford (MIPS),
Department of Radiology and Bio-X Program,
1201 Welch Rd, P093,
Stanford, CA 94305-5484, USA
Tel: +1 650 725 0950; Fax: +1 650 736 7925;
E-mail: shawchen@stanford.edu